Energy Conversion and Management 337 (2025) 119900

Contents lists available at ScienceDirect

Energy Conversion and Management

journal homepage: www.elsevier.com/locate/enconman

Research Paper

Solar thermal assisted proton exchange membrane electrolyzer and solid oxide fuel cell system based on biomass gasification for green power and hydrogen production: Multi-objective optimization and exergoeconomic analysis

Shayan Sharafi Laleh [a], Haniyeh Sadat Rezaei Mousavi [a], Shayan Rabet [a], Farnaz Nojavan [b], Mortaza Yari [a], Saeed Soltani [c,*]

[a] Department of Mechanical Engineering, University of Tabriz, Tabriz, Iran
[b] Department of Mechanical Engineering, University of Utah, Salt Lake city 84112 UT, USA
[c] Faculty of Engineering and Natural Sciences, Antalya Bilim University, 07190 Antalya, Turkey

ARTICLE INFO

Keywords:
Biomass Gasification
SOFC
PEME
Green hydrogen
Solar thermal
Multi-objective optimization

ABSTRACT

The industrial revolution led to technological advances but also exacerbated environmental issues, notably increasing carbon emissions. This study introduces a novel hybrid system combining photovoltaic-thermal (PVT), proton exchange membrane electrolyzer (PEME), gasification, solid oxide fuel cell (SOFC), and a Rankine cycle to address these challenges. The system features solar-assisted gasification with preheated air and water to improve syngas quality, increasing hydrogen content and enhancing combustion efficiency. The PEME unit uses excess solar electricity for green hydrogen production, ensuring a flexible clean fuel source, while oxygen produced by the PEME is injected into the SOFC cathode, improving electrochemical performance. This integrated system operates entirely on biomass-derived syngas, reducing reliance on fossil fuels. Comprehensive energy, exergy, and economic analyses confirm the system's potential, achieving 55.03 % energy efficiency and 50.64 % exergy efficiency, with a product cost of $0.125/kWh. A multi-objective optimization study showed an energy efficiency of 74.88 %, reducing the environmental impact to 0.24 kg/kWh. The results highlight the system's ability to optimize performance, cost-effectiveness, and environmental sustainability, offering a promising solution for industrial decarbonization.

1. Introduction

1.1. Preface

The industrial revolution catalyzed unparalleled technological progress while simultaneously presenting considerable environmental issues. The excessive carbon emissions from industrial activities have intensified the greenhouse effect, leading to increased frequency and severity of meteorological events [1]. In response to this urgent challenge, fuel cells offer a viable solution by facilitating the conversion of gaseous fuels into power and heat via an electrochemical process. This technique, unlike conventional combustion systems limited by the Carnot cycle, produces significantly reduced emissions [2]. Solid oxide fuel cells (SOFCs), employing solid oxide materials as the electrolyte, can directly utilize diverse fuel gases, hence improving efficiency by reducing energy losses and pollutant emissions [3]. Biomass is becoming acknowledged as a feasible substitute for fossil-derived feedstocks in the production of fuel and chemicals. Biomass, derived from renewable sources such as trees, crops, grasses, algae, and agricultural byproducts, provides a sustainable method for energy generation. Lignocellulosic biomass, mostly consisting of lignin, cellulose, and hemicellulose, presents significant potential owing to its structural constituents. Transforming biomass into hydrogen-rich gas is among the most effective methods for its utilization; nonetheless, biomass with a moisture content exceeding 70 % necessitates specific conversion processes [4]. The quest for sustainable fuels derived from plentiful resources is crucial for the progress of the energy sector. The conversion of fossil fuels and greenhouse gases into valuable molecules, particularly with the incorporation of renewable energy, facilitates the emergence of hydrogen and syngas

* Corresponding author.
E-mail addresses: soltani929@gmail.com, saeed.soltani@antalya.edu.tr (S. Soltani).

https://doi.org/10.1016/j.enconman.2025.119900
Received 16 February 2025; Received in revised form 7 April 2025; Accepted 4 May 2025
Available online 12 May 2025

Nomenclature

Abbreviations

A	The solar collector area (m^2)
AB	After Burner
AC	Air Compressor
b	Width of PVT collector (m)
$c_{p,\ total}$	Total specific cost per unit exergy ($/GJ)
$\dot{C}$	Cost rate ($/h)
CC	Combustion Chamber
CRF	Capital Recovery Factor
D	Membrane thickness
E	Reversible potential
E_0	Electromotive force (V)
$E_{electric}$	Input electricity (kW)
$\dot{E}x$	Exergy flow rate (kW)
$\dot{E}x_D$	Exergy destruction (kW)
F	Faraday's constant
g	Specific Gibbs free energy
GT	Gas Turbine
h	Specific enthalpy (kJ/kg)
h_{P1G}	Penalty factor from solar cell material, glass, and EVA in glass-to-glass PVT
h_{P2G}	Interface penalty between glass and fluid via absorber in glass-to-glass PVT
HHV	Higher Heating Value (kJ/kg)
HX	Heat Exchanger
i_r	Interest rate
I	Resultant current
$\dot{I}$	Solar radiation intensity(W/m^2)
J	Current density
J_i^{ref}	Pre-exponential factor
K	Equilibrium constant
L	Thickness of a cell component
LHV	Lower Heating Value (kJ/kg)
$\dot{m}$	Mass flow rate(m/s)
MC	Moisture content per mole of wood
n	Operational years
N_{FC}	Number of cells in PEM electrolyzer
P	Pressure (kPa)
PEM	Proton Exchange Membrane
PVT	Photo Voltaic Thermal
$\dot{Q}$	Heat transfer rate(kW)
$\overline{R}$	Universal gas constant (kJ/kg K)
R_C	Resistivity of the content
R_{PEM}	Total ohmic resistance
s	Specific entropy (kJ/kg K)
SOFC	Solid Oxide Fuel Cell
Syngas	Synthesis gas
T	Temperature (K)
U_F	Fuel utilization factor
U_L	Overall heat loss coefficient of the solar collector (kW/m^2K)
U_0	Heat loss coefficient between the ambient and receiver of the solar collector (kW/m^2K)
V_0	Reversible Potential
V	Overall losses
$\dot{W}$	Consumed/Produced power (kW)
w	Quantity of water per kilomole of biomass
y	Mole fraction (mol)
Z	Cost function ($)
$\dot{Z}$	Investment cost rate ($/hr)

Greek Symbols

α_b	Absorptivity of the black surface
α_c	Absorptivity of solar cell
β_c	Packing factor of solar cell
ζ_{Env}	environmental impact factor
η	Efficiency
λ	Membrane-electrode water content
ρ	Electrical resistivity
σ_{PEM}	Proton conductivity in PEM (S/m)
τ_g	Transmissivity of the glass

Subscripts and Superscripts

0	Standard atmospheric conditions
a	Anode
act	Activation
c	Cathode
ch	Chemical
CI	Capital Investment
conc	Concentration
eff	Effective
OM	Operation and Maintenance
ohm	Ohmic
imp	Impurities
conc	Concentration

as reliable energy carriers [5]. Alongside hydrogen production by photoelectrolysis, various techniques such as hydrocarbon reforming, coal or biomass gasification, thermal decomposition, and thermochemical water splitting are being investigated to satisfy increasing hydrogen demand. Solar energy, extensively utilized for its scalability and ease of installation, constitutes a vital element of the renewable energy sector. The generation of hydrogen using water electrolysis, especially with excess renewable energy sources, presents significant potential [6]. Various energy storage technologies, such as electrical, electrochemical, mechanical, thermal, and chemical systems, are utilized across different sizes and discharge durations, classified as short-term, medium-term, or long-term storage solutions [7]. Water electrolysis is distinguished as a genuine "green hydrogen" technology, demonstrating considerable potential in three principal methods: alkaline, solid oxide, and PEM (Proton Exchange Membrane) electrolysis [8]. PEM electrolysis is distinguished by its exceptional efficiency, swift reactivity, and compatibility with renewable energy sources [9]. Incorporating innovative thermal cycles, such as the Organic Rankine and Kalina cycles, with solar thermal collectors is an effective approach for sustainable power production [10]. Nevertheless, solar energy systems have the intrinsic difficulty of inconsistent energy generation rates over the day, influenced by varying sunshine availability [11]. A hybrid solar-powered energy system that co-generates electricity and hydrogen may be utilized across various industrial applications, showcasing the viability of these systems for extensive and dependable energy production [12].

1.2. Previous works

A solar thermal system with a gas turbine, PCM-supported MFD, PEME, and TEG is presented by Demir et al. [13] This increases H_2 to 129.9 kg/day, when PEME temperature is raised. At 267.9 kW, TEG reaches its maximum 7.11 %. The system produces 1210 tons of water per day, 50.6 GJ of electricity per day, and an energy efficiency of 42.5 % and 40.5 %, respectively. Ma et al. [14] propose a H_2 generation system utilizing PVT and a PEME. The efficiency of PVT-PEME rises with

Table 1
A review of recent literature review with products and main findings.

Reference	Year	Energy source	Feature of system	Analysis methods	Energy products	Main findings
Salari et al. [26]	2024	Solar	– PVT – PEM	– Energy – Exergy – ANN-based Optimization	H_2 O_2 DHW Power	– In spring: 2.10 mol/h, summer: 2.22 mol/h, fall: 1.93 mol/h, winter: 1.87 mol/h – the respective maximum H_2 production rates – The Arithmetic Optimization Algorithm stands out as a superior type of ANN, demonstrating exceptional accuracy.
Ogorure et al. [21]	2024	Biomass	– Gasification – PEM – SOFC	– Energy – Exergy – Economic – MOGA optimization	H_2 Power	– Total power output is 9.05 MW – Produce H_2 of 0.0023 kg/s with PEME efficiency of 73.73 %.
Tera et al. [27]	2024	Dry biomass	– Gasification – SOFC	– Energy – Exergy – Emergy	H_2 Power	– The emergy study indicated that the system relies on procured inputs. – Inexpensive, low-carbon power can amount to 58.42 million dollars.
Ishaq et al. [28]	2019	Biomass Solar	– Gasification – PVT	– Energy – Exergy – Economic	Power H_2 O_2	– A H_2 production rate of 59.45 mol/s and a power output of 8.3 MW are generated. – The overall energy and exergy efficiencies are determined to be 29.9 % and 31.5 %, respectively.
Zheng et al. [24]	2023	Solar	– PVT – PEM – SOFC	– Energy – Exergy – Economic – Environmental	Power	– As the receiver side length of the PTPVT fluctuates from 0.04 m to 0.08 m, the electric efficiency of the PTPVT diminishes from 24.19 % to 22.93 %. – The grid power usage of the hybrid system escalates by 16.62 MWh annually.
Saberi Mehr et al. [25]	2024	Solar Biomass	– PV – PEM – SOFC – Gasification	– Energy – Exergy – Economic – Environmental – Optimization	Power H_2	– The mixture of H_2 with syngas enhances combined heat and power efficiency by as much as 3 %.
Present work	2025	Solar Biomass	– PVT – PEM – SOFC – Gasification	– Energy – Exergy – Economic – Environmental – Optimization	Power H_2	– Improved syngas composition via water–gas shifting and gasidication agent preheating that enhances SOFC performance. – Achieving 55.03 % energy efficiency and 50.64 % exergy efficiency, with a product cost of $0.125/kWh.

ambient temperature, but that of PV-PEME declines. The efficiency of the electrolyzer reaches its maximum at elevated irradiation intensity and diminishes with increased incoming flow, whereas the efficiency of PVT-PEME increases. Elevated temperatures diminish PV efficiency while enhancing PEME performance; conversely, the system exhibits reduced efficiency in cold, low-irradiance environments. Soyturk et al. [15] develop a hybrid system of 20 PVT panels, a PEME, H_2 storage, and PEM for an off-grid residence. The system employs 8 batteries and 29.4 kg hydrogen tanks to fulfill energy requirements, utilizing H_2 as a power source from December to April.

Liu et al. [16] propose a solar-assisted system utilizing ammonia-fueled SOFC with anode outlet gas recirculation. During summer, exergy efficiency is 47.83 % with a primary energy saving of 51.36 %; in winter, they are 50.52 % and 52.01 %, respectively. Solar collectors and gas recirculation diminish fuel consumption and improve efficiency. A hybrid concentrated solar thermal and biomass gasification system that produces 0.8 million MWh yearly and saves 787.7 kg CO_2-eq/ton of waste wood is evaluated by Fang et al. [17] Despite an NPV of €-0.7 billion over 30 years, they suggest a 20 % gain in efficiency and a 19 % decline in O&M costs. According to Forootan et al. [18], a solar-CH_4 system with SOFC and PEME produces 201.6 kg/h of H_2, 49.48 % energy efficiency, 47.21 % exergy efficiency, and 133 MW of electricity. System efficiency and hydrogen production are improved by SOFC and PEME. Zhao et al. [19],provides a PEMEC-SOFC system with 367.92 kWh/m^3 of storage density, 54.29 % energy efficiency, and 50.34 % exergy performance. A rising in SOFC temperature results in a 12.02 % rise in energy utilization.

A SOFC-based cogeneration and co-gasification system with 44.70 % effectiveness, 162.02 kW of electricity, and 52.41 kW of heat is presented by Yang et al. [20] In the SOFC, efficiency losses are 19.99 %, whereas in the gasifier, they are 24.43 %. Using a TSOFC set at 852 °C, 25 % litter, and 0.73 fuel, the energy efficiency is 41.95 %, and the cost per GJ is 42.35$.

Ogorure et al. [21] created a biomass system that included PEME, SOFC, and gasification. PEME upgrades syngas from 4.20 to 37.78 MJ/kg by producing 0.0023 kg/s of hydrogen. The plant's energy efficiency is 54.81 %, its energy efficiency is 44.87 %, its production is 9.05 MW, and its cost is $111.8/MWh. A biomass gasification system for a SOFC, PEME, and desalination is presented by Abedinia et al. [22], which achieves 53.66 % energy, 38.2 % exergy efficiency, 377.6 kW, and 0.1633 kg/s freshwater. Straw and CO_2 boost energy efficiency to 42.71 %, with a $6.29/GJ product cost, $1.65 million in income, and payback time of 4.01 years. Yin et al. [23] devised a sludge-based supercritical water gasification-supercritical water oxidation-SOFC system including solar thermal energy consumption. The SOFC attains an efficiency of 48.76 %, whilst the system obtains energy and exergy efficiencies of 63.16 % and 56.20 %, respectively. Profitability is achieved in 2.59 years, providing both economic and environmental benefits. Zheng et al. [24] assert that a solar-driven CCHPS system incorporating PEMEC, SOFC, and PTPVT collector achieves an electric efficiency of 24.19 % and a sustainability index of 0.998. An increase in PTPVT size results in a decrease in efficiency to 22.93 % and an augmentation of grid use by 16.62 MWh/year.

Saberi Mehr et al. [25] utilize thermal solar (PV) to energize a PEME, generating green H_2; a gasifier transforms waste into syngas for a SOFC. With 21.17 % H_2, CHP efficiency increases by 3 %, CO_2 emissions decrease, and costs climb. At 973 K and 5445 A/m^2, the exergy efficiency attains 53.29 %.

Table 1 presents a thorough examination of contemporary literature, revealing diverse arrangements of energy systems that include subsystems including Solid Oxide Fuel Cells, Photovoltaic-Thermal units, Proton Exchange Membrane electrolyzers, and biomass gasification. Among the reviewed studies, Saberi Mehr et al. stands out as it integrates all four of these subsystems within a single framework.

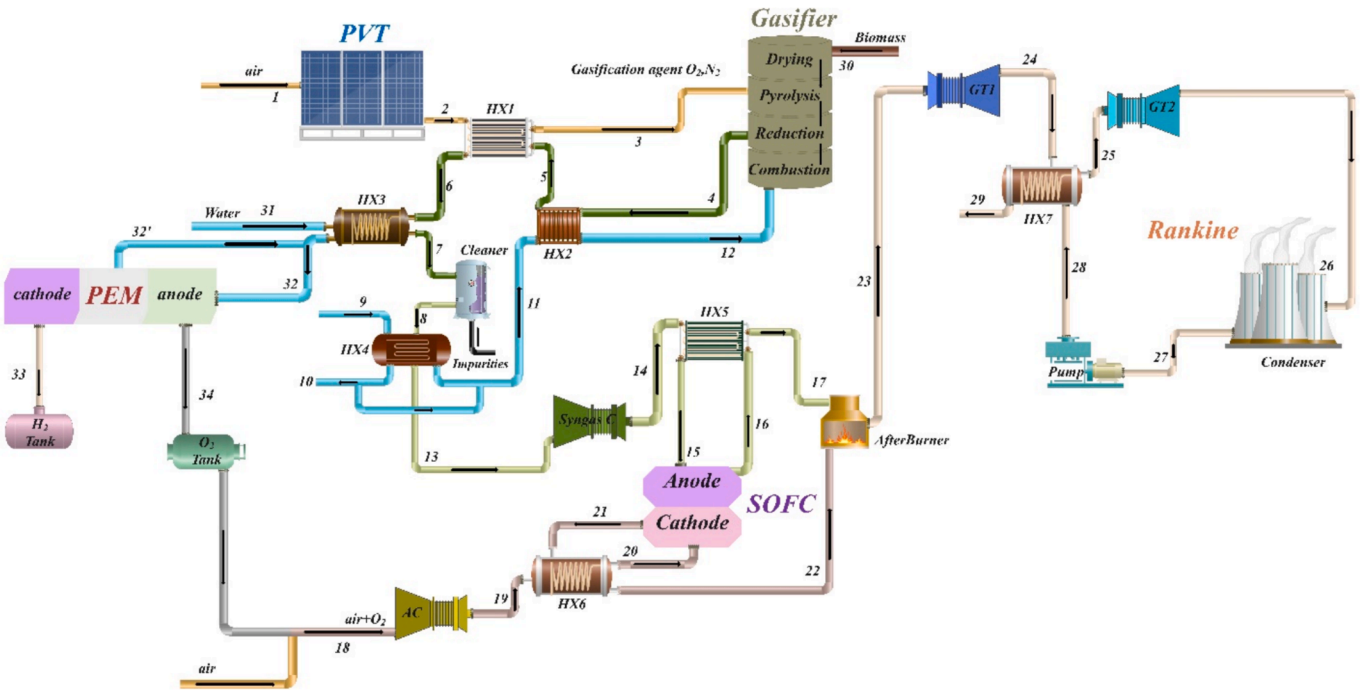

Fig. 1. Thermodynamic Configuration of the Suggested System.

Nevertheless, the drawbacks of the previous studies are highlighted in present work which include the absence of preheating the input air in the gasification process utilizing the PVT subsystem, which signifies a lost chance for enhancing system efficiency. Moreover, our proposed system distinctly integrates the water–gas shift reaction within the gasification unit, thereby augmenting the hydrogen content of the syngas and fostering a more efficient and sustainable overall framework.

The significant contributions and benefits of our configuration are comprehensively examined in the Merits of the Study subsection.

1.3. Merits of study

This system integrates photovoltaic-thermal (PVT), proton exchange membrane electrolyzer (PEME), gasification, solid oxide fuel cell (SOFC), and Rankine cycle technologies to enhance efficiency and sustainability. The main novelty lies in the solar-assisted gasification, hydrogen production, and optimized SOFC operation, leading to a high-efficiency, low-emission poly-generation system. The key contributions are as follows:

- Preheating gasification agents (air and water) using solar thermal energy and syngas preheating improves syngas quality. This increases hydrogen content, enhances combustion efficiency, and reduces tar formation.
- Improved syngas composition enhances SOFC performance. A higher hydrogen-to-carbon ratio leads to greater power output and better fuel utilization.
- Green hydrogen is produced via a PEME unit using excess solar electricity. This provides a clean fuel source for various applications.
- Solar electricity powers PEME, while solar heat preheats gasification air. This dual use of solar energy maximizes system efficiency.
- Stored hydrogen ensures reliability, while PEME-generated oxygen enhances SOFC performance. Higher oxygen purity improves electrochemical reactions and reduces nitrogen dilution.
- Biomass is used as the sole SOFC fuel, ensuring a fully renewable energy source. This reduces reliance on fossil fuels and lowers emissions.
- Optimized gas injection into SOFC electrodes improves performance and longevity. Precise control minimizes side reactions and enhances stability.
- Multi-objective optimization confirms the system's thermodynamic and economic viability. The best trade-offs between efficiency, hydrogen production, and cost-effectiveness are identified.

By integrating these innovations, the proposed system offers a sustainable, efficient, and clean energy solution with lower carbon emissions, higher fuel utilization, and reduced dependency on fossil fuels.

2. System description and assumptions

This section illustrates the configuration and operation of the proposed system, comprising a photovoltaic thermal (PVT) unit, a gasifier, a solid oxide fuel cell (SOFC), a proton exchange membrane electrolyzer (PEME), and a Rankine cycle. As illustrated in Fig. 1, air enters the PVT system at state 1, where it is preheated, exiting at state 2. The preheated air then passes through Heat Exchanger 1 (HX1) and exits at state 3, reaching the required temperature for the gasification process. Concurrently, water enters HX3 at state 31, where it is preheated to the operating temperature of the PEM unit at state 32. The preheated water is then fed into the PEM unit, which receives energy from the PVT system to electrolyze the water, producing hydrogen and oxygen at states 33 and 34, respectively.

In parallel, water enters HX4 at state 9, where it is heated further. A portion of this water passes through HX2, transitioning from states 11 to 12, and is then injected into the gasifier. Biomass enters the gasification unit at state 30, where it reacts with the preheated air and water, producing syngas at state 4. The syngas passes sequentially through HX2, HX1, and HX3 (states 5 to 7), transferring heat to preheat water and air, before entering the cleaner unit at state 7 to remove impurities.

Following impurity removal, the syngas exits at state 8 and is compressed in the syngas compressor at state 13 to achieve the necessary pressure for SOFC operation. The compressed syngas is further preheated in HX5, transitioning from state 14 to state 15, and then enters the SOFC anode to produce power. The unreacted fuel exits the SOFC at state 16, passes back through HX5 to transfer heat, exits at state 17, and

Table 2
Detailed Exploration of Research Model Assumptions.

Parameter and Unit	Value	Ref.
Reference pressure, P_0 (atm)	1	–
Reference temperature, T_0 (K)	298.15	–
Solar thermal		
Packing factor of solar,β_c	0.83	[29]
Transmissivity of glass,τ_g	0.95	[29]
Overall heat transfer coefficient, U_L (W/m^{2}K)	4.71	[29]
Penalty factor due to presence of interface between glass and working fluid through absorber plate,h_{P2G}	0.189	[29]
Penalty factor due to presence of solar cell material, glass and EVA,h_{P1G}	0.9782	[29]
Absorptivity of black surface,α_b	0.9	[29]
Absorptivity of solar cell,α_c	0.85	[29]
Temperature of sun, T_{sun} (K)	4500	[29]
Solar radiation intensity, İ (kW/m^2)	1	[29]
Width of PVT collector, b	40	–
PEME		
Temperature of PEM, T_{PEM} (K)	353	[30]
Pre-exponential factor of anode, J_a^{ref}(A/m^2)	1.7 × 10^5	[30]
Pre-exponential factor of cathode, J_c^{ref}(A/m^2)	4.6 × 10^3	[30]
Faraday constant, F (C/mol)	96,486	[30]
Area of PEM, A_{PEM} (m^2)	0.0232	[30]
Membrane thickness, D (μm)	50	[30]
Water content at anode-membrane interface,λ_a	14	[30]
Water content at cathode- membrane interface,λ_c	10	[30]
Activation energy of anode, $E_{act,a}$ (kJ/mol)	76	[30]
Number of cells, N	785	[30]

enters the afterburner.

Simultaneously, oxygen from the PEM unit's O_2 tank and air from the environment are compressed together in the air compressor, transitioning from state 18 to state 19. The pressurized air is preheated in HX6, exiting at state 20, and enters the SOFC cathode. After participating in the electrochemical reaction, the air exits the SOFC at state 21, passes back through HX6 to transfer heat, exits at state 22, and enters the afterburner.

In the afterburner, the unreacted syngas from state 17 and the air from state 22 are burned, producing high-temperature, high-pressure exhaust gases at state 23. These gases expand through Gas Turbine 1 to generate power, exiting at state 24, and transfer heat in HX7 before entering Gas Turbine 2 at state 25. After expanding in Gas Turbine 2, the gases are condensed in the condenser at state 26, exiting as liquid at state 27. The condensed liquid is then pressurized by a pump, exiting at state 28, and re-enters HX7 to complete the Rankine cycle, exiting at state 29.

This integrated system effectively utilizes waste heat and optimizes energy conversion to achieve high efficiency and low environmental impact.

3. System modeling

This paper uses EES for simulation and MATLAB for optimization of the studied model, incorporating comprehensive evaluations of mass, energy, exergy, and economic impacts based on thermodynamic principles. The section also outlines a multi-objective optimization strategy. Table 2 provide detailed explanations of the key assumptions underlying the models used in this study.

3.1. Thermodynamic modeling and analysis

The existing system is simulated under the assumption of a stable state, considering the pressure decrease throughout the system while neglecting the kinetic and potential energy of each separate flow. This part attempts to conduct an analysis by precisely defining the system and its separate components in terms of thermodynamic properties. The steady-state parameters for energy, and mass are represented by Eqs. (1) and (2) [31].

$$\sum \dot{m}_{in} - \sum \dot{m}_{out} = 0 \tag{1}$$

$$\dot{Q} - \dot{W} = \sum (\dot{m}h)_{in} - \sum (\dot{m}h)_{out} \tag{2}$$

Table A1 in the appendix displays the equilibrium energy mathematical formulas for the overall system.

Table 3
Equilibrium Constants for reactions [33].

	Shift	Reforming
A	5.47302×10^{-11}	-2.63122×10^{-11}
B	-2.57478×10^{-7}	1.24067×10^{-7}
C	4.63741×10^{-7}	-2.25233×10^{-7}
D	-3.91501×10^{-1}	1.95027×10^{-1}
E	11.2096	−66.1396

3.1.1. SOFC modeling

For a solid oxide fuel cell (SOFC) powered by methane, Either methods of internal or external reforming approaches are employed. The reaction mechanism of the SOFC stack with internal reforming can be described as follows [32]:

$$a_r \rightarrow [CH_4 + H_2O \leftrightarrow CO + 3H_2](Reforming) \tag{3}$$

$$b_r \rightarrow [CO + H_2O \leftrightarrow CO_2 + H_2](Shifting) \tag{4}$$

$$c_r \rightarrow \left[H_2 + \frac{1}{2}O_2 \leftrightarrow H_2O\right](Overallelectrochemicalreaction) \tag{5}$$

The rates at which the molar conversion occurs for Eqs. (3)–(5) are denoted as a_r, b_r and c_r, respectively.

The hydrogen used in the fuel cell can be represented as follows [32]:

$$c_r = U_F(3a_r + b_r) \tag{6}$$

U_F represents the variable that indicates the efficiency with which fuel is utilized in the system.

The proportion of air effectively used in a process for reactions, excluding non-reactive purposes (air utilization ratio) can be calculated as [32]:

$$U_O = \frac{c_r}{2\dot{n}_{O_2,3}} \tag{7}$$

The rate of substance flow in moles of the gases are obtained by applying mass balances based on Eqs. (3)–(5) (refer to Table 3). The variable $\dot{n}$ represents the rate of molar flow. The molar concentartions of the elements are provided in Table 3, where *y* represents the concentration of each component in the flow.

The following is an expression for the equilibrium constants for the shift and reforming processes, respectively [32]:

$$K_r = \frac{y_{CO,12} \times y^3{}_{H_2,12}}{y_{CH_4,12} \times y^3{}_{H_2O,12}} \left(\frac{P_{12}}{P_{ref}}\right)^2 = \frac{\dot{n}_{CO,12} \times \dot{n}^3{}_{H_2,12}}{\dot{n}_{CH_4,12} \times \dot{n}^3{}_{H_2O,12}} \left(\frac{P_{12}}{\dot{n}_{12} \times P_{ref}}\right)^2 \tag{8}$$

$$K_s = \frac{y_{CO_2,12} \times y_{H_2,12}}{y_{CO,12} \times y_{H_2O,12}} = \frac{\dot{n}_{CO_2,12} \times \dot{n}_{H_2,12}}{\dot{n}_{CO,12} \times \dot{n}_{H_2O,12}} \tag{9}$$

The equilibrium constants K_r and K_s exhibit a direct correlation with temperature [33].

$$logK = AT^4 + BT^3 + CT^2 + DT + E \tag{10}$$

The values for A, B, C, D, and E can be found in Table 3.

3.1.1.1. Actual voltage. The disparity in the thermodynamic potentials of the electrode reactions establishes the reversible cell voltage, commonly referred to as the emf (electromotive force). The emf can be precisely specified by the Nernst equation [32]:

$$E_0 = -\frac{\Delta\bar{g}^0}{2F} + \frac{\bar{R}.T_{FC,e}}{2F} ln\left(\left(\frac{y_{H_2,12} \times \sqrt{y_{O_2,12}}}{y_{H_2O,12}}\right) \times \sqrt{\frac{P_{12}}{P_{ref}}}\right) \quad (11)$$

Where

$$\Delta\bar{g}^0 = \bar{g}^0_{H_2O} - \bar{g}^0_{H_2} - \frac{1}{2}\bar{g}^0_{O_2} \quad (12)$$

$$\bar{g}^0 = \bar{h} - T_{FC,e}.\bar{s}^0 \quad (13)$$

In this context, $\Delta\bar{g}^0$ represents the Gibbs free energy, $\bar{R}$ stands for the universal gas constant $\left(8.314\frac{J}{mol.K}\right)$, $T_{FC,e}$ refers to the temperature at the exit of the SOFC, and F represents the Faraday constant $\left(96485\frac{^{\circ}C}{g.mol}\right)$. Furthermore, $\bar{h}$ represents t4he enthalpy per unit of molar flow rate, while $\bar{s}^0$ denotes the standard entropy per unit of molar flow rate. For ideal gases, the reduced Planck constant $(\bar{h})$ varies with temperature, while the molar entropy $(\bar{s}^0)$ varies with temperature and the standard pressure [32].

The Nernst voltage refers to the highest attainable voltage in a fuel cell while there is no electrical current passing through it. The voltage of a cell is reduced from its open-circuit voltage due to polarization losses, and can be mathematically represented as [32]:

$$V_C = E_0 - (\eta_{ohm} + \eta_{act} + \eta_{conc}) \quad (14)$$

The variables η_{ohm}, η_{act} and η_{conc} represent the activation polarization, ohmic polarization, and concentration polarization, respectively.

3.1.1.2. Ohmic polarization. Ohmic polarization is a crucial factor in all fuel cell types and is defined by Bossel and Dubal [34] in the following manner:

$$\eta_{ohm} = (R_C + \rho_C L_C + \rho_a L_a + \rho_e L_e + \rho_{int} L_{int}).j \quad (15)$$

Where

$$\rho_e = \left(3.34 \times 10^4 exp\left(-10300/T_{FC,e}\right)\right)^{-1} \quad (16)$$

$$\rho_a = \left(95 \times 10^6/T_{FC,e} exp\left(-1150/T_{FC,e}\right)\right)^{-1} \quad (17)$$

$$\rho_c = \left(42 \times 10^6/T_{FC,e} exp\left(-1200/T_{FC,e}\right)\right)^{-1} \quad (18)$$

$$\rho_{int} = \left(9.3 \times 10^6/T_{FC,e} exp\left(-1100/T_{FC,e}\right)\right)^{-1} \quad (19)$$

In this context, R_C represents the resistivity of the contact, ρ denotes the electrical resistivity of the cell components, L represents the thickness of a cell component, and j refers to the current density. The subscripts *ohm*, *c*, *a*, *e* and int represent the terms ohmic, cathode, anode, electrolyte, and interconnect, respectively.

3.1.1.3. Activation polarization. Activation polarization occurs when the energy barriers for a reaction at the electrode–electrolyte interface are overcome. Kim et al. [35] expresses the losses due to activation polarization as follows:

$$\eta_{act} = \eta_{act,a} + \eta_{act,c} \quad (20)$$

Where

$$\eta_{act,a} = \frac{\bar{R}.T_{FC,e}}{F}.\left(sinh^{-1}\left(\frac{j}{2j_{0a}}\right)\right) \quad (21)$$

$$\eta_{act,c} = \frac{\bar{R}.T_{FC,e}}{F}.\left(sinh^{-1}\left(\frac{j}{2j_{0c}}\right)\right) \quad (22)$$

In this context, j_{0a} represents the exchange current density of the anode, while j_{0c} represents the exchange current density of the cathode.

3.1.1.4. Concentration polarization. During the passage of electric current, concentration gradients form, resulting in varying concentrations of species at the boundaries between the three phases. These differences in concentration lead to losses in concentration. The losses are particularly noticeable when fuel or oxidant gasses with poor levels of purity are supplied to the fuel cell stack. Chan et al. [36] define concentration polarization in the following manner:

$$\eta_{conc} = \eta_{conc,a} + \eta_{conc,c} \quad (23)$$

Where

$$\eta_{conc,a} = \frac{\bar{R}.T_{FC,e}}{2F}.\left(ln\left(1 + \frac{P_{H_2}.j}{P_{H_2O}.j_{as}}\right) - ln\left(1 - \frac{j}{j_{as}}\right)\right) \quad (24)$$

$$\eta_{conc,c} = -\left(\frac{\bar{R}.T_{FC,e}}{F}.ln\left(1 - \frac{j}{j_{cs}}\right)\right) \quad (25)$$

$$j_{as} = \frac{2F.P_{H_2}.D_{aeff}}{\bar{R}.T_{FC,e}.L_a} \quad (26)$$

$$j_{cs} = \frac{4F.P_{O_2}.D_{ceff}}{\left(\left(\frac{P_4 - P_{O_2,4}}{P_4}\right)\bar{R}.T_{FC,e}.L_c\right)} \quad (27)$$

In this context, D_{aeff} represents the effective diffusion of gas via the anode, while D_{ceff} represents the effective diffusion of gas through the positive electrode (cathde).

3.1.1.5. The solid oxide fuel cell-generated power. The work rate produced by the solid oxide fuel cell (SOFC) stack can be calculated in the following manner [32]:

$$\dot{W}_{FC,stack} = N_{FC}.I.V_c \quad (28)$$

N_{FC} represents the quantity of cells, while I denotes the resultant current. The resulting current I and current density j can be expressed as [32]:

$$I = j.A_a \quad (29)$$

$$j = \frac{2FC_r}{N_{FC}.A_a} \quad (30)$$

In this context, A_a represents the active surface area, while C_r refers to the rate of molar conversion related to the total electrochemical reaction mechanism $H_2 + \frac{1}{2}O_2 \rightarrow H_2O$.

3.1.2. Biomass gasification and reforming

The gasification process involves converting biomass into a syngas mixture by allocated oxidation in partial amounts. Syngas, consisting mainly of CO, H_2, and CH_4, is a very useful conduit energy that can be used for generating electricity, producing heat, and synthesizing biofuels. The equilibrium model posits that all gasifier reactions should ultimately approach thermodynamic equilibrium. The pyrolysis products are intended to undergo combustion and achieve a state of balance in the reduction zone prior to exiting the gasifier. The reactions described below take place in the reduction zone [37,38]:

Table 4
Equalization for proton exchange membrane electrolyzer [30].

Total obtained energy	$\Delta H = \Delta G + T\Delta S$
Hydrogen mass flow rate	$\dot{N}_{H2,out} = \frac{J}{2F} = \dot{N}_{H2O,reacted}$
Input electricity	$E_{electric} = JV$
Overall losses	$V = V_0 + V_{act,a} + V_{act,cath} + V_{ohm}$
The reversible potential	$V_0 = 1.229 - 8.5 \times 10^{-4}(T_{PEM} - 298)$
Local ionic conductivity	$\sigma_{PEM}[\lambda(x)] = [0.5139\lambda(x) - 0.326]exp\left[1268\left(\frac{1}{303} - \frac{1}{T}\right)\right]$
Membrane-electrode water content	$\lambda(x) = \frac{\lambda_a - \lambda_c}{D}x + \lambda_c$
Total ohmic resistance	$R_{PEM} = \int^{D}_{0} \frac{dx}{\sigma_{PEM}[\lambda(x)]}$
Ohmic overpotential	$V_{ohm,PEM} = JR_{PEM}$
Activation overpotential	$V_{act,i} = \frac{RT}{F} sinh^{-1}\left(\frac{J}{2J_{0,i}}\right), i = a, cath$
Exchange current density	$J_{0,i} = J_i^{ref} exp\left(-\frac{E_{act,i}}{RT}\right), i = a, cath$

Table 5
Expression for Thermodynamic assessment of photo voltaic system [29].

interpretation	Factors
Heat rate of through glasses	$\dot{Q}_{solar} = \frac{\dot{m}_{air}Cp_{air}}{U_L}\left(h_{P2G}Z\dot{I}\right) - U_L(T_{air,in} - T_0)\left[1 - exp\left(\frac{-bU_L L}{\dot{m}_{air}Cp_{air}}\right)\right]Z = \alpha_b\tau_g{}^2(1-\beta_c) + h_{P1G}\tau_g\beta_c(\alpha_c - \eta_c)$
Generation of power	$W_{PVT} = \eta_c I\beta_c\tau_g A$
Temperature of exit air	$T_{air,output} = \left(T_0 + \frac{h_{P2G}Z\dot{I}}{U_L}\right)\left[1 - \frac{1 - exp(\frac{-bU_L L}{\dot{m}_{air}Cp_{air}})}{\frac{-bU_L L}{\dot{m}_{air}Cp_{air}}}\right]\left[T_{air,in}\frac{1 - exp(\frac{-bU_L L}{\dot{m}_{air}Cp_{air}})}{\frac{-bU_L L}{\dot{m}_{air}Cp_{air}}}\right]$
Effectiveness of energy	$\eta_{PV/T} = \frac{\dot{Q} + \dot{W}_{PV/T}}{\dot{I}bU_L}$

$$C + CO_2 \leftrightarrow 2CO \tag{31}$$

$$C + H_2O \leftrightarrow CO + H_2 \tag{32}$$

$$C + 2H_2 \leftrightarrow CH_4 \tag{33}$$

$$CO + H_2O \leftrightarrow CO_2 + H_2 \tag{34}$$

The equilibrium constant for methane production is [37,38]:

$$K_1 = \frac{P_{CH_4}}{\left(P_{CH_4}\right)^2} \tag{35}$$

The value for the shift response is [37,38]:

$$K_2 = \frac{P_{CO_2}P_{H_2}}{P_{CO}P_{H_2O}} \tag{36}$$

Zainal et al. [37] have provided the following expression to represent the gasification reaction in downdraft gasifiers:

$$C_XH_YO_Z + wh_2O + m(O_2 + 3.76N_2) \rightarrow n_1H_2 + n_2CO + n_3CO_2 + n_4H_2O + n_5CH_4 + n_6N_2 \tag{37}$$

In Eq. (37), per kilomole of biomass, w and m denote the amounts of H_2O and O_2.Wood, the chosen biomass, is primarily made up of C, H, and O, featuring a higher heating value (HHV) of $449568kJ/kmol$ and a composition of $CH_{1.44}O_{0.66}$, according to Zainal et al. [37] MC represents the Per mole of wood, moisture level, defined by the equation [37,38]:

$$MC = \frac{18w}{24 + 18w} \tag{38}$$

Therefore,

$$w = \frac{24MC}{18(1 - MC)} \tag{39}$$

Given that MC is assumed to be constant, w is regarded as being immutable. The constants for CH_4 production and the water–gas shift processes can be calculated from the biofuel coefficient data, as provided in [37,38] for Eq. (40) and Eq. (41).

$$K_1 = \frac{n_5}{(n_1)^2} \tag{40}$$

And

$$K_2 = \frac{n_3n_1}{n_2n_4} \tag{41}$$

The whole combustion reaction in the CC is described by the following equation [37,38]:

$$n_1H_2 + n_2CO + n_3CO_2 + n_4H_2O + n_5CH_4 + n_6N_2 + n_{air}(O_2 + 3.76N_2) \rightarrow n_7CO_2 + n_8H_2O + n_9O_2 + (n_6 + 3.76n_{air})N_2 \tag{42}$$

Further insights into the gasification method are available in the research by Zainal et al. [37] and Soltani et al. [38].

3.1.3. PEM electrolyzer

The PEM electrolyzer comprises three primary constituents: the anode, electrolyte, and cathode. These devices work by using electricity in order to assist the injected H_2O oxidize, yielding protons and O_2 at the negative electrode (anode) and electrons and H_2 at the electrode called the cathode. While the O_2 is released, the H_2 derived is kept in the storage [39]. Table 4 comprises a compilation of equalization required for the representation and simulation of these systems. For more specific and comprehensive information about PEM electrolyzers, refer to the research conducted by Ahmadi et al. [30].

3.1.4. Solar thermal

Considering the top and back surfaces of the insulation, the computation calculates a total coefficient of heat transfer (U_L) via the cell's surface and the outdoors. The capacity for absorption of the photovoltaic cell is α_c, in comparison to that of the black surface is α_b. The contact area across the layer of glass and the fluid that flows along the surface of the absorber, alongside the presence of glass and ethylene–vinyl acetate in the glass-to-glass PVT system, are the causes of the penalty quantities h_{P2G} and h_{P1G} . The PVT system's equations have been modeled, simulated, and the outcomes are shown in Table 5. The system supplies power for hydrogen synthesis and heats the air necessary to facilitate biomass gasification. The PVT packaging coefficient (β_c), a transmission value (τ_g) values, and PVT glass's effectiveness of solar cells (η_c), and have been listed in the Table 5. The total surface of the solar collection agencies, indicated by (A) [29].

3.2. Exergy analysis

The foundations of the 2nd law of thermodynamics and the concepts of energy and mass conservation are combined in energy assessment. When assessing the rate of which useable energy is wasted inside a system, the exergy balance formula highlights the significance of what is called the dead state temperature (T_0) and the boundary temperature (T_j) of the entire structure [40].

In a steady-state control volume, the exergy conservation equation is:

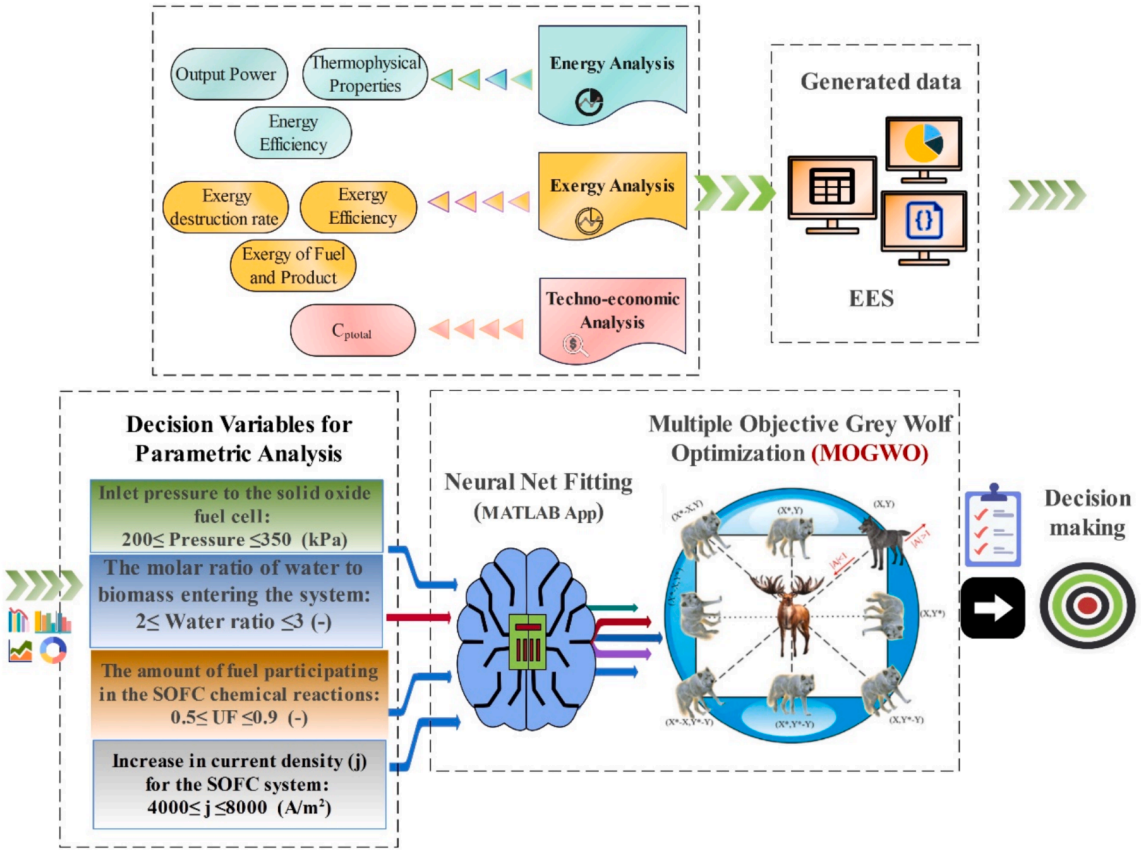

Fig. 2. The schematic illustrates the overall simulation and optimization process.

$$\sum_{inlets}\dot{E}_i+\sum\dot{Q}_j\left(1-\frac{T_0}{T_j}\right)=\sum_{outlets}\dot{E}_e+\dot{W}_{CV}+\dot{I}_{CV} \tag{43}$$

In this equation, the term $\sum\dot{Q}_j\left(1-\frac{T_0}{T_j}\right)$ signifies the transfer of exergy associated with heat transfer, while $\dot{I}_{CV}$ denotes the internal irreversibility inherent in the process. The overall exergy transfer of the fluid used for operation, $\dot{E}$, which incorporates both mechanical and chemical contributions, is established by the exergy rates associated with the system's entry and exits, indicated by $\sum_{inlets}\dot{E}_i$ and $\sum_{outlets}\dot{E}_e$, consecutively.

$$\dot{E}=\dot{E}_{th}+\dot{E}_{ch} \tag{44}$$

The subsequent equation is used to calculate the thermomechanical exergy transfer for the fluid in operation.

$$\dot{E}_{th}=\sum\dot{m}_i[(h_i-h_0)-T_0(s_i-s_0)] \tag{45}$$

The chemical exergy transfer for a mixture of ideal gases can be computed using the formula below.

$$\dot{E}_{ch}=\dot{m}\left(\sum y_i\bar{e}_i^{ch,0}+\overline{R}T_0\sum y_i\ln(y_i)\right) \tag{46}$$

Table A2 in appendix shows the system's exergy conservation formulas.

3.3. Exergoeconomic analysis

The price associated with the components used in the cogeneration system is given in Table B1 in appendix.

Each component's overall expense frequency is equal to the sum of its repair and renovation and investment rates [40]:

$$\dot{Z}_k=\dot{Z}_k^{CI}+\dot{Z}_k^{OM} \tag{47}$$

The below formula provides the investment expense portion [40]:

$$\dot{Z}_k^{CI}=\frac{CRF}{\tau}Z_k \tag{48}$$

The definition of CRF is [41],while τ is the yearly hours:

$$CRF=\frac{i_r(1+i_r)^n}{(1+i_r)^n-1} \tag{49}$$

The interest rate is symbolized by i_r in this formula, and the amount of operation years by n.

The subsequent calculation provides the upkeep price rate [41]:

$$\dot{Z}_k^{OM}=\frac{\gamma_k Z_k}{\tau} \tag{50}$$

Since the component's upkeep factor has been indicated by γ_k.

The cogeneration system's overall expenses rate is [42]:

$$\dot{Z}_{tot}=\sum\dot{Z}_k \tag{51}$$

3.4. Performance criteria

The system energy efficiency is determined as:

$$\eta_{energy}=\frac{W_{net}+\dot{W}_{solar}+n_{p,H_2}LHV_{H_2}}{LHV_{biomass}+\dot{I}b_{solar}I_{solar}+\dot{E}_{elec}} \tag{52}$$

The calculation of system exergy efficiency is as follows:

Table 6
Present model vs. Tao et al. [43] and Yari et al. [44].

Current density J(A/cm^2)	Cell voltage V_{cell}(V) (present work)	Cell voltage V_{cell}(V) (Tao et al. [43])	Cell voltage V_{cell}(V) (Yari et al. [44])	Density of power (W/m^2) (present work)	Density of power (W/m^2) (Tao et al. [43])	Density of power (W/m^2) (Yari et al. [44])
0.2	0.787	0.76	0.742	0.154	0.15	0.148
0.3	0.702	0.68	0.684	0.215	0.21	0.205
0.4	0.64	0.62	0.634	0.251	0.26	0.253
0.5	0.551	0.57	0.582	0.283	0.295	0.294
0.6	0.513	0.52	0.547	0.304	0.315	0.328

Table 7
Present model vs. Zainal et al. [37].

Ingredient	Present study	Zainal [37]
O_2	0.01	0.00
H_2	18.03	21.06
N_2	48.71	46.68
CO_2	13.86	12.01
CO	18.79	19.61
CH_4	0.65	0.64

$$\eta_{exergy} = \frac{W_{net} + \dot{E}_{product_{PVT}} + \dot{E}_{17} + \dot{E}_{H_2}}{\dot{E}_{elec} + \dot{E}_{16} + \dot{E}_{ch_{biomass}} + WE_{ch_{air}} + \dot{I}b_{solar}I_{solar}} \quad (53)$$

An alternate definition of the system's levelized cost of goods is:

$$C_{P,total} = \frac{\dot{Z}_{combined} + \dot{C}_{fuel}}{W_{net} + \dot{W}_{solar} + \dot{E}_{H_2}} \quad (54)$$

Calculating the environmental efficiency of energy systems through CO_2 absorption and hydrogen energy inputs:

$$\zeta_{Environmental} = 3600\left(\frac{n_{CO_2,ab}.MolarMass(CO_2)}{W_{net} + \dot{W}_{solar} + n_{p,H_2}LHV_{H_2}}\right) \quad (55)$$

3.5. Multi-objective optimization

The Multi-Objective Grey Wolf Optimizer (MOGWO) is a sophisticated optimization technique tailored for improving energy conversion applications. The modeling steps and the optimization process employed in this study are thoroughly illustrated in Fig. 2.

The objective functions in this study comprise energy efficiency, total specific cost, and the environmental impact factor. Similar to other optimization techniques, the MOGWO method relies on defined decision-making parameters. The decision variables considered in this analysis are as follows:

- Inlet pressure to the solid oxide fuel cell:$200 \leq Pressure \leq 350(kPa)$

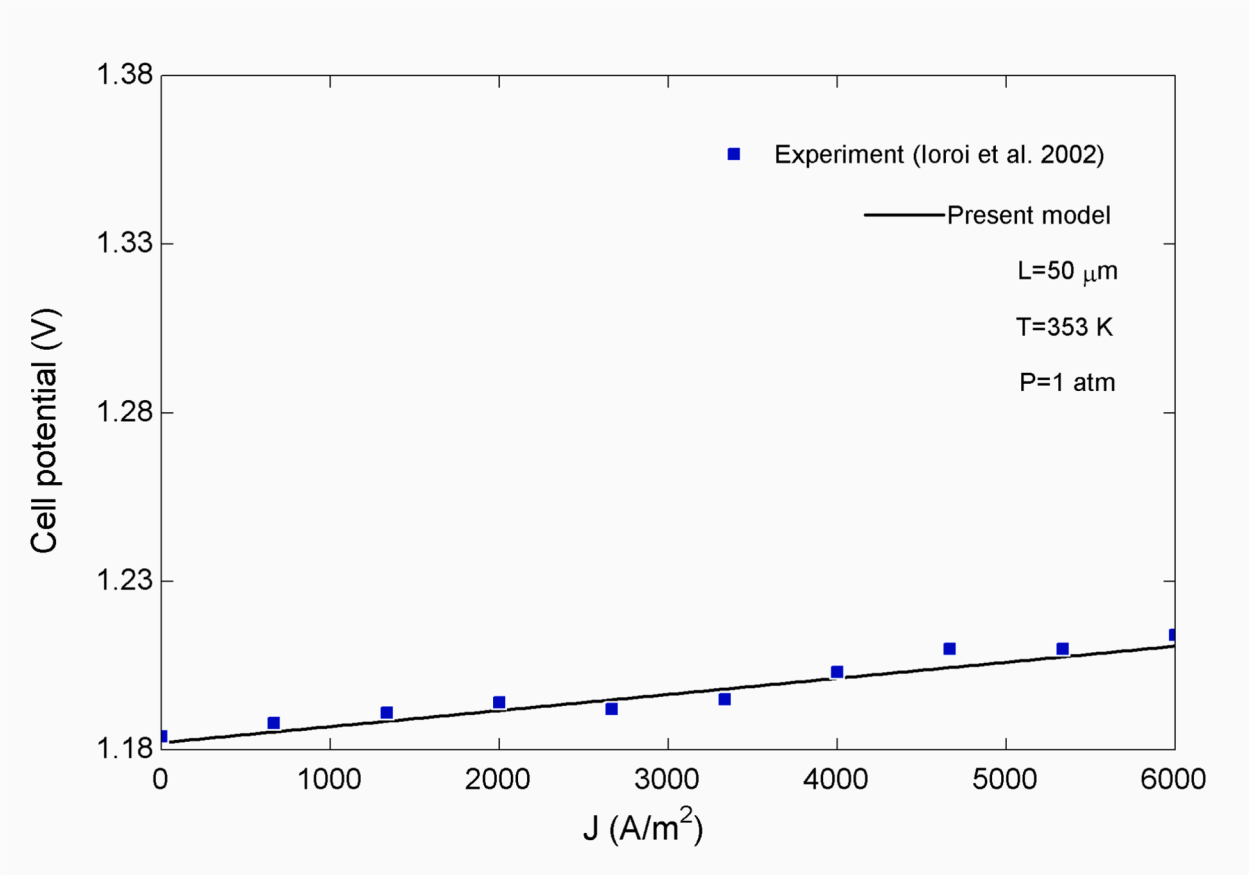

Fig. 3. Validation of PEME and comparison with the results of Loroi et al. [45].

Table 8
Thermodynamic Characteristics of States.

No. of state	T(K)	P(kPa)	ṁ(kg/s)	H(kJ/kmol)	S(kJ/kmol.K)	Ėx(kW)
1	298.3	101.1	0.0505	4.366	194.3	0
2	314.4	101.1	0.0505	471.9	195.9	0.02226
3	900	100.9	0.0505	18,437	227.9	14.69
4	1073	100.6	0.2455	−84181	215.8	2493
5	970.2	100.4	0.2455	−87997	212.1	2457
6	905.7	100.2	0.2455	−90351	209.6	2436
7	350	100	0.2455	−109121	177.9	2312
8	350	99.9	0.2455	−97495	176.4	2472
9	298.2	101.3	0.1649	−241811	188.7	0
10	338.2	101.2	0.1649	−240462	193	0.7337
11	346	101.2	0.04504	−240196	193.7	0.2855
12	900	100.9	0.04504	−219880	228.3	25.27
13	320	99.7	0.265	−98423	173.7	2310
14	424.4	255.1	0.265	−95157	174.7	2347
15	1000	250	0.265	−75455	203.9	2481
16	1100	245	0.3187	−167522	229.1	1220
17	626.8	244.8	0.3187	−185961	207.3	1064
18	298.3	101.3	2.023	4.366	194.5	0
19	406.2	265.3	2.023	3163	195.5	199.6
20	1000	260	2.023	21,738	223.6	912.9
21	1100	254.8	1.93	25,023	226.5	1030
22	489.9	244.8	1.93	5645	201.3	233.3
23	908	239.9	2.249	−26185	222.7	884.3
24	755.3	102.3	2.249	−31353	223.5	459.8
25	650	5000	0.2606	56,548	118.2	309.1
26	315	8.163	0.2606	8521	11.48	74.9
27	314.7	8	0.2606	3132	10.67	0.447
28	315.3	5000	0.2606	3261	10.8	1.787

- The molar ratio of water to biomass entering the system:$2 \leq Waterratio \leq 3(-)$
- The amount of fuel participating in the SOFC chemical reactions:$0,5 \leq UF \leq 0,9(-)$
- Increase in current density (j) for the SOFC system:$4000 \leq j \leq 8000(A/m^2)$

4. Verification of model

The accuracy of the Solid Oxide Fuel Cell (SOFC) model is validated by comparing it with both the experimental data from Tao et al. [43] and the simulation results from Yari et al. [44]. As shown in Table 6, the model demonstrates good agreement with both sources, particularly in terms of the relationship between current density (J), cell voltage (V_{cell}), and power density.

Previously pointed out, the suggested downdraft gasifier operates in an equilibrium constant, which is in line with the outcomes of the investigation done by Zainal et al. [37]. The method of confirmation identified by demonstrating a gasifier employing wood as the biomass, and the validated model's output is compared to Zainal's assessment [37] in Table 7.

Fig. 3 displays the cell potential-current density profile of the electrolyzer for the assessed configuration together with the outcome of Ioroi et al.'s experimental investigation [45].

5. Results and discussion

For comparison analysis, Table 8 shows the results for several system states, including ṁ(kg/s), Ėx(kW), and the specific thermodynamic parameters of the fluids used for operation. The provided input data comprises a Fuel Utilization Factor (UF) of 0.8 and a current density (j) of 8000 A/m^2.

Based on the case study of the system, the overall output power and energy efficiency are determined to be 1395 kW and 55.03 %, respectively, while the exergy efficiency is 50.64 %, demonstrating the system's effective utilization of energy and exergy resources. The supplies' cost estimate is 0.125 $/kWh, highlighting the system's economic feasibility. For individual units within the system, the energy efficiency values are as follows: the SOFC achieves an efficiency of 24.88 %, the gas turbine (Rankine cycle) exhibits a significantly high efficiency of 89 %, and the PVT system attains an efficiency of 31.79 %. These results emphasize the contribution of each component to the overall

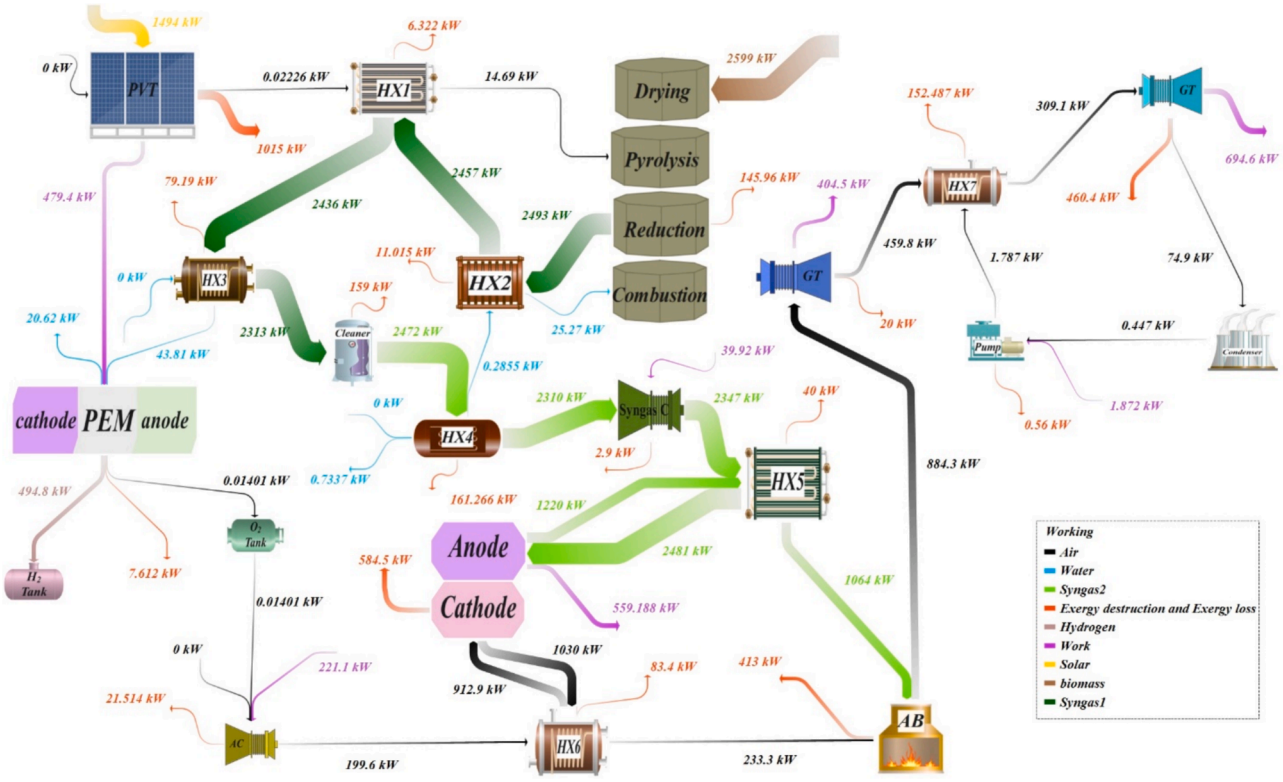

Fig. 4. Sankey diagram of system components.

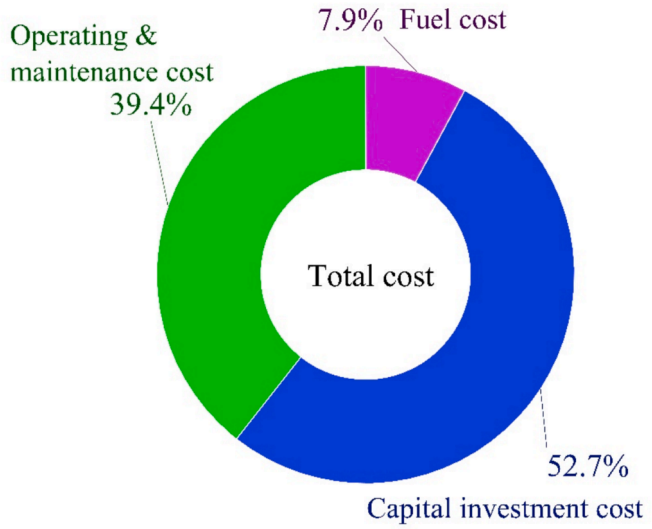

Fig. 5. Total cost distribution.

performance and sustainability of the integrated system.

Fig. 4 illustrates the Sankey diagram of exergy flows for the system in the case study. The diagram highlights the exergy balance within each system component, detailing the input, output, destruction, and losses of exergy. Solar and biomass exergy are utilized within the SOFC cycle to enhance power generation. Notably, exergy destruction is minimized due to the use of waste heat to perform work in the SOFC. Additionally, the output power from the PVT system is directed to the PEM cycle for hydrogen production. The highest exergy destruction occurs in the PVT system, followed by the SOFC and the Gas turbine of the Rankine cycle and the afterburner, respectively. However, due to the preheating of input syngas for the SOFC using waste heat, exergy destruction within the SOFC is significantly reduced.

To assess the economic viability of the proposed hybrid poly-generation system, both capital and operational expenditures were analyzed. Fig. 5 shows the total cost distribution. As illustrated in Fig. 5, the total cost distribution reveals that capital investment accounts for 52.7 %, followed by operating and maintenance (O&M) costs at 39.4 %, and fuel cost comprising only 7.9 % of the total, assuming a biomass price of 2 USD/GJ.

In Fig. 6, a detailed breakdown of the capital and O&M costs by component is presented. The Photovoltaic-Thermal (PVT) system represents the largest share, constituting 59.72 % of the total cost. This is followed by:

- Heat Exchanger 6 (HX6): 44.65 %
- Heat Exchanger 7 (HX7): 32.63 %
- Gas turbine (after Afterburner): 18.35 %
- Heat Exchanger 5 (HX5): 16.23 %
- Proton Exchange Membrane Electrolyzer (PEME): 14.54 %
- Solid Oxide Fuel Cell (SOFC): 7.375 %

The remaining components each contribute less than 7 % to the overall cost.

This analysis highlights the scalability of the system by identifying cost-intensive components and their relative economic impact. Moreover, the relatively low sensitivity of the system to fuel cost fluctuations, due to the low fuel share (7.9 %), emphasizes its economic resilience, especially under varying biomass prices. This reinforces the system's potential for sustainable implementation in small-scale and off-grid applications, where fuel price volatility is a concern.

The proposed system is analyzed through a parametric study to observe how its performance varies with changes in key parameters.

Preheating the gasification agent air in a biomass gasifier is critical for enhancing both the chemical and performance aspects of the gasification process. From a chemical perspective, preheating increases the initial temperature of the air, which facilitates endothermic reactions such as pyrolysis and char gasification, leading to a more efficient breakdown of biomass into syngas components like hydrogen, carbon monoxide, and methane. Higher temperatures also reduce tar formation, improving syngas quality. Performance-wise, preheating reduces the external energy required to sustain the gasification process, thereby improving thermal efficiency and reducing operational costs. As is evident in Fig. 7, as the temperature of the gasification agent rises, correspondingly increases the quantity of H_2 and CO. All the other elements decrease in quantity, which helps achieve syngas with higher

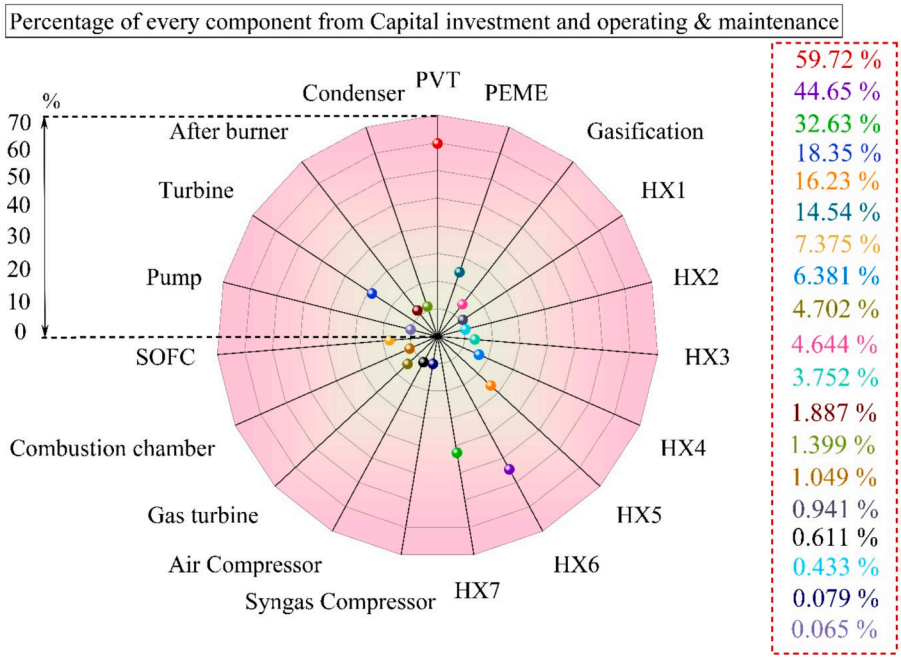

Fig. 6. Percentage of every component from capital investment and operating & maintenance costs.

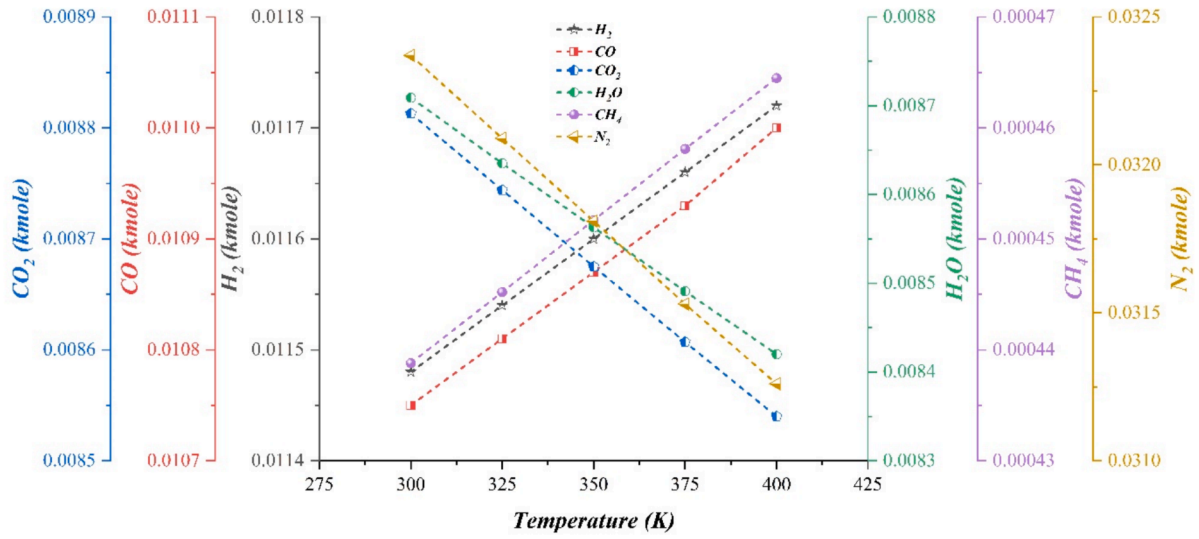

Fig. 7. The effect of air preheating on syngas quality.

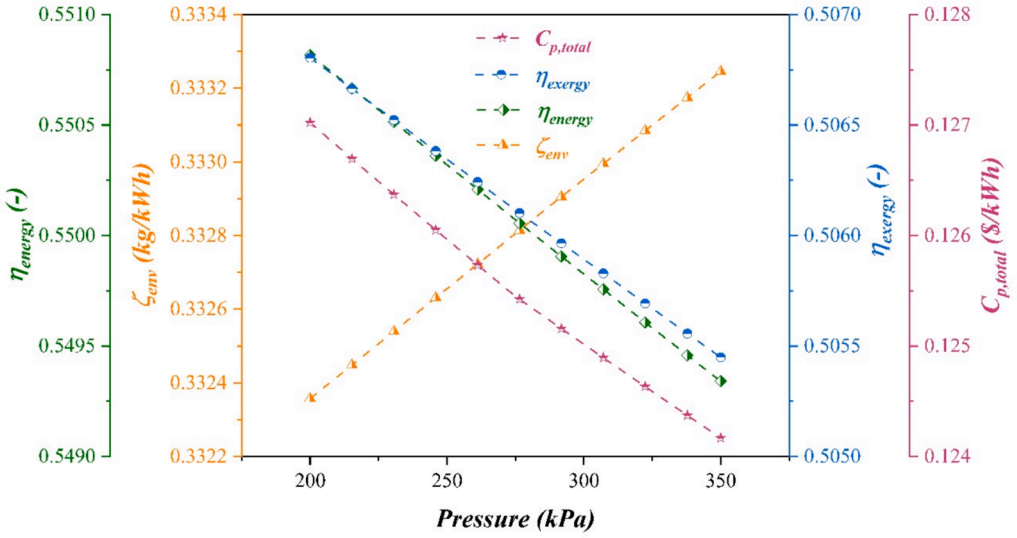

Fig. 8. Variations of inlet pressure to the solid oxide fuel cell.

quality. Although methane is on a decreasing trend with this enterprise, it is noteworthy that methane is far more scarce in the syngas mix and its effect is negligible.

Fig. 8 illustrates the variation in inlet pressure to the solid oxide fuel cell (SOFC) within the range of 200 to 350 kPa. As shown, increases in the environmental index (ζ_{Env}) contrast with the decreasing trends in energy, exergy efficiencies and total cost of products ($C_{p,total}$). Overall, raising the SOFC inlet pressure negatively impacts system performance. This is primarily due to the increased power consumption of compressors, which the system's power generation cannot sufficiently offset. Consequently, the total power output, as well as the energy, exergy efficiencies and total cost of products ($C_{p,total}$), decline.

Fig. 9 presents the molar ratio of water to biomass entering the system, which directly affects hydrogen production and, subsequently, the chemical composition of the SOFC inlet, impacting its performance. By increasing the water ratio from 2 to 3, the after-burner temperature decreases, thus reducing the heat input to the gas turbine. This approach is employed in the system as an alternative to water injection or pump usage for SOFC water addition, facilitating methane reforming. As the water ratio increases, the environmental index (ζ_{Env}) and total cost ($C_{p,total}$) rise, while the energy and exergy efficiencies decrease.

Fig. 10 shows the amount of fuel participating in the SOFC chemical reactions, indicating that as the Fuel Utilization Factor (*UF*) increases from 0.5 to 0.9, methane in the SOFC anode outlet products is completely eliminated, reflecting the extent of fuel conversion. Additionally, the amount of H_2 that is electrochemically converted depends on the *UF*. With an increase in *UF*, the ζ_{Env} and $C_{p,total}$ indicators show an increasing trend, while energy and exergy efficiencies decrease. This result may be true for a combined power system that benefits from bottoming cycles because of heat recovery of the exhaust gases from the afterburner. In this proposed model, the gas turbine and the Rankine cycle may benefit more from quality combustion in the afterburner compared to the SOFC unit.

Fig. 11 shows that, as indicated, with an increase in current density (*j*) for the SOFC system from 4000 to 8000 A/m2 all system parameters exhibit an increasing trend. For example, energy and exergy efficiencies rise due to the increase in the system's power output, which is a result of the increased heat load entering the gas turbine, thereby raising the total power output. Conversely, the ζ_{Env} and $C_{p,total}$ indicators show a decreasing trend.

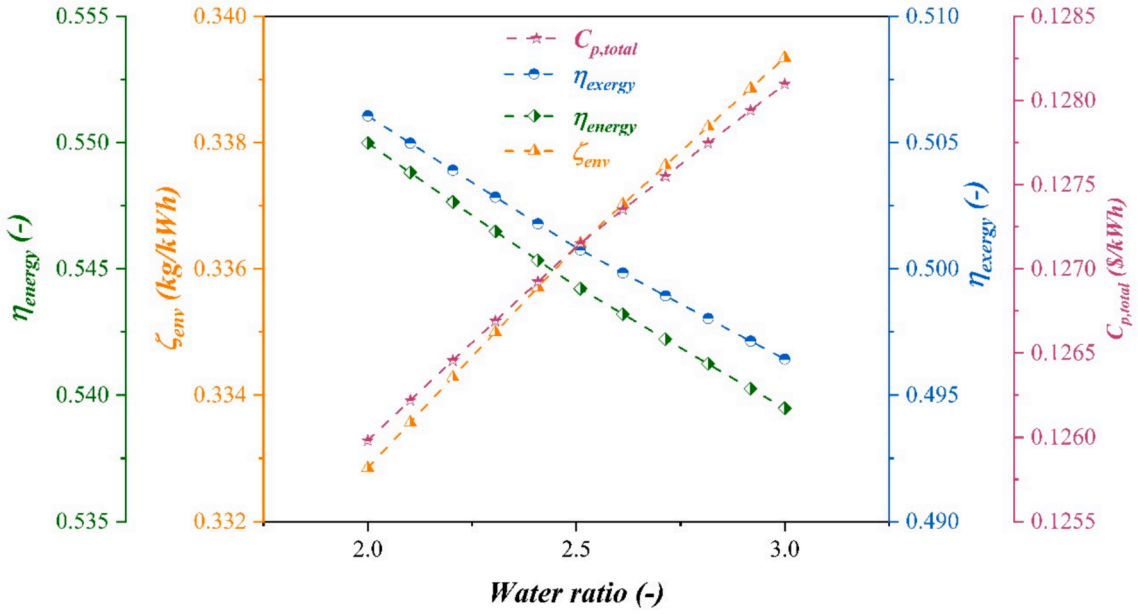

Fig. 9. Variations in the water ratio to enhance system performance.

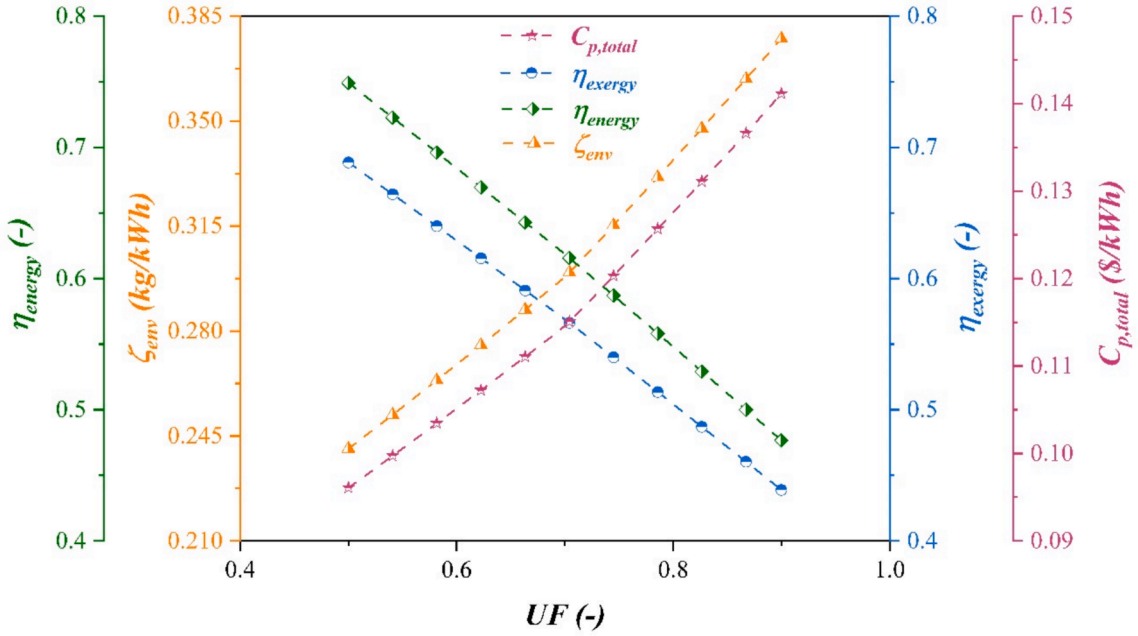

Fig. 10. Variations in the Fuel Utilization Factor (*UF*) to enhance system performance.

Fig. 12 illustrates the impact of biomass moisture content on the overall performance of the system. As depicted in the Fig. 12, increasing the moisture content leads to a rise in the energy required to heat the biomass to the gasification temperature. This is due to the additional energy needed to evaporate the higher water content present in the biomass. Consequently, the molar fractions of nitrogen, water vapor, and carbon dioxide increase. This occurs because a greater amount of air is required to supply the necessary energy, which introduces more nitrogen into the system. Furthermore, the elevated moisture content leads to higher production of water vapor and CO_2. These effects are detrimental to system performance, as they reduce the heating value of the syngas and increase the energy losses, ultimately lowering the overall efficiency of the system.

Fig. 13 presents the effect of varying solar radiation intensity on system efficiency. As shown in the Fig. 13, an increase in solar radiation leads to a higher net output power from the photovoltaic-thermal (PVT) unit. However, when evaluating the system based on energy and exergy efficiencies, the contribution of the PVT system remains relatively low. This is because only a small portion of the increased solar energy is effectively converted and integrated into the overall system performance.

Moreover, in calculating the emission index and the cost of products, the solar input is not accounted for as a primary energy source within the system boundaries. As a result, increasing solar radiation intensity indirectly improves the emission index and reduces the cost of products, since the additional output is achieved without increasing fossil fuel consumption or operational cost, thereby enhancing the system's environmental and economic performance.

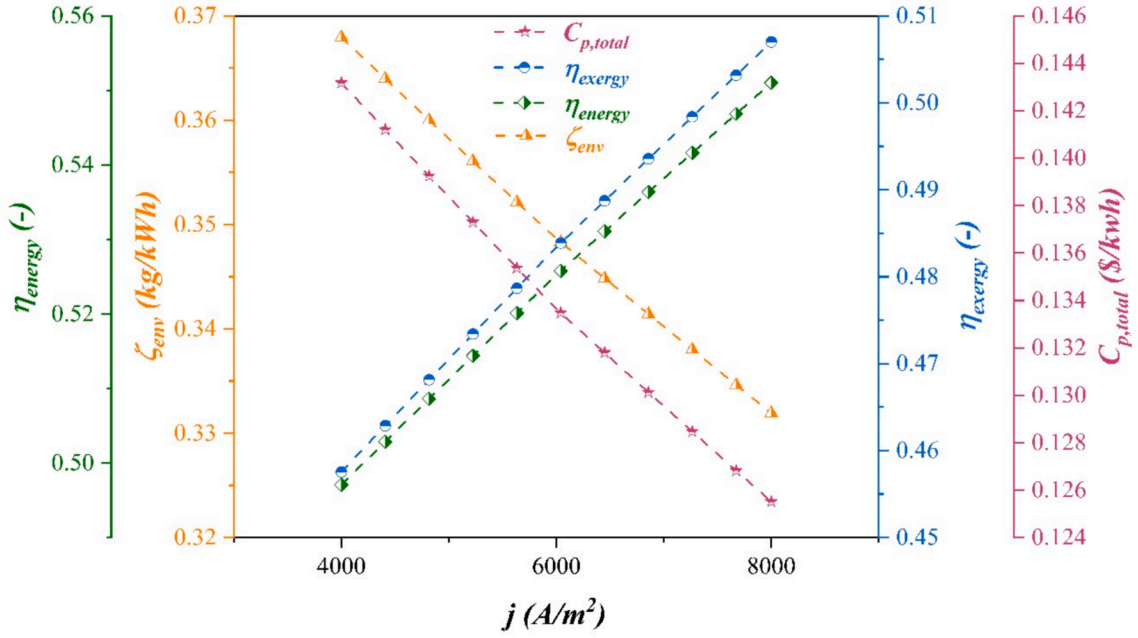

Fig. 11. Variations in the current density to enhance system performance.

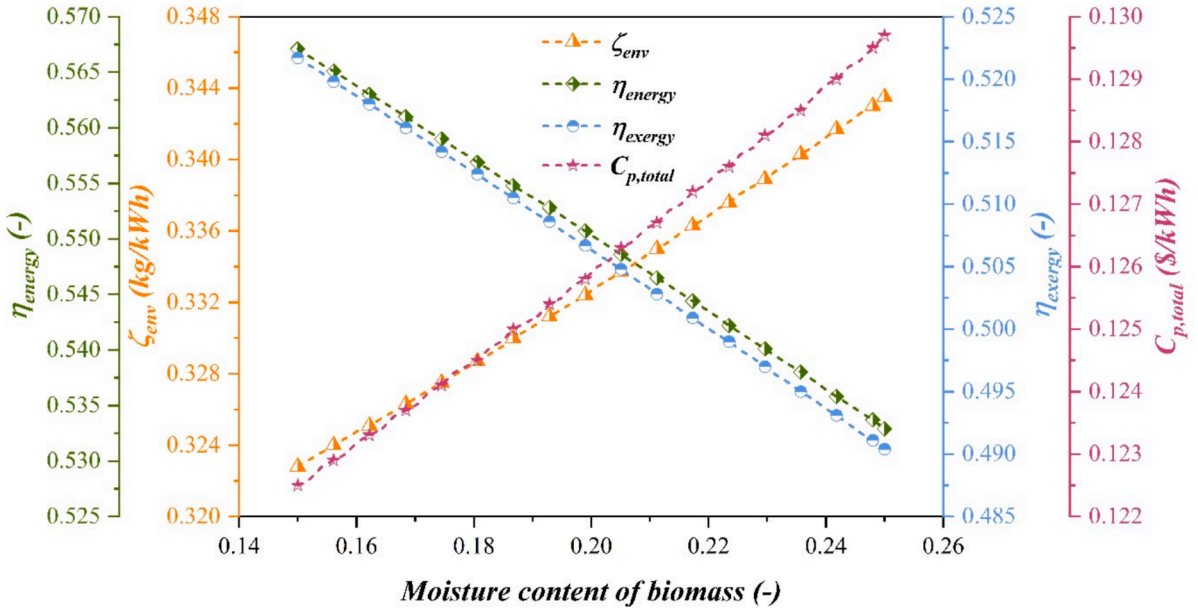

Fig. 12. Variations of the biomass moisture content on the overall performance.

Following the completion of the parametric study, the system optimization analysis is conducted. The Pareto front diagrams are first examined to visualize the trade-offs among the optimization objectives. This is followed by a detailed analysis of the population distribution diagram for the four key parameters assessed in the parametric study, providing insights into their influence on the optimization process.

Fig. 14 illustrates the Pareto front diagram, which represents the trade-off relationships between total specific cost ($C_{p,total}$), energy efficiency (η_{energy}), and environmental impact factor (ζ_{Env}). Each point on the curve reflects a compromise between these parameters, indicating the degree to which improving one objective might affect the others. Optimal values obtained from this analysis are $C_{p,total}$=0.098 $/kWh, η_{energy}=74.84 %, andζ_{Env} = 0.244 kg/kWh balancing cost efficiency, energy performance, and environmental impact.

Fig. 15 shows the second scenario, where the goal is to maximize energy and exergy efficiency while minimizing the C_p. In this case, the C_p, energy, and exergy efficiency all have clear value correspondences. Optimal values obtained from this analysis are $C_{p,total}$=0.098 $/kWh, η_{energy}=74.84 %, andη_{exergy} = 68.78 % balancing cost efficiency, energy and exergy performance.

The last optimization scenario as shown in Fig. 16 seeks to minimize the C_p and environmental impact factor while maximizing exergy efficiency. Environmental impact factor, exergy efficiency, and C_p are computed as 0.244 kg/kWh, 68.77 %, and 0.098 $/kWh in this case, respectively.

The Scatter distribution in Figs. 17a–17l provides insight into the key parameters influencing system performance across three optimization scenarios. Each subfigure illustrates the distribution of critical

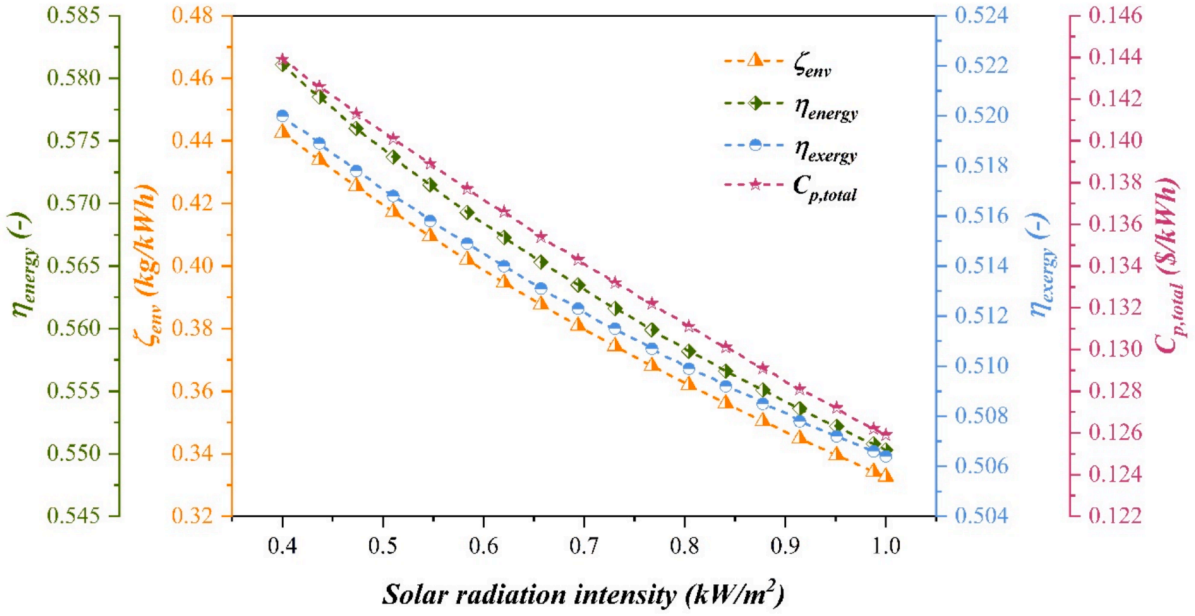

Fig. 13. Variations of the solar radiation intensity on the overall performance.

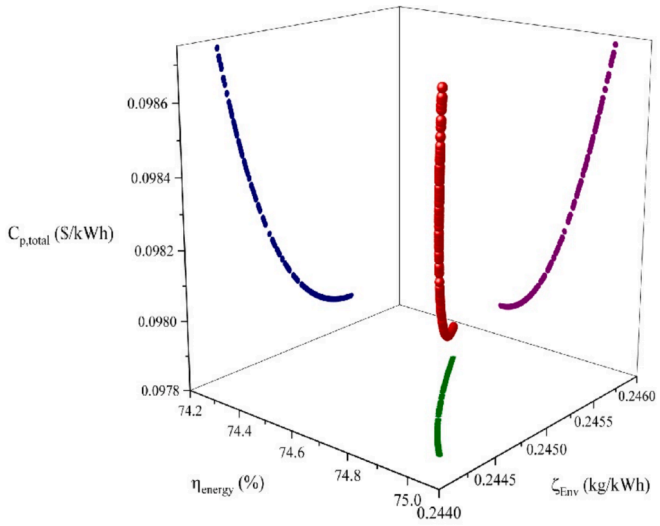

Fig. 14. The Pareto front diagram for first scenario.

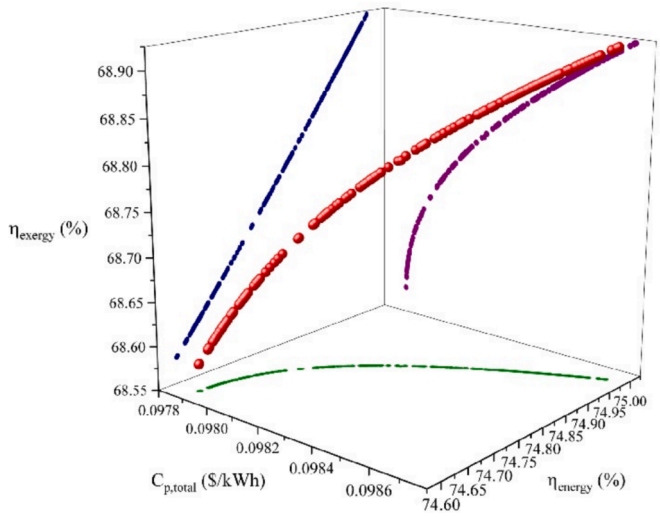

Fig. 15. The Pareto front diagram for second scenario.

parameters, highlighting the optimal values that emerge from the optimization process.

In the first optimization scenario Figs. 17a–17d, the key parameters analyzed include the utility fuel factor (UF), inlet pressure, water ratio in gasification, and SOFC current density. The results indicate that the inlet pressure clusters between 200 and 275 kPa, suggesting this range as optimal. The water ratio is most frequently observed at 2, implying it as the preferred value. Similarly, the utility fuel factor converges around 0.5, and the current density clusters at 8000 A/m^2, marking these as optimal operating conditions.

The second optimization scenario Figs. 17e–17h yields similar results, reaffirming the identified optimal ranges. Likewise, the third scenario Fig. 17i–17l follows the same trend, further validating the robustness of these values across different optimization settings. The results demonstrate that the inlet pressure can vary between 200 and 275 kPa, the water ratio remains at 2, the utility fuel factor stabilizes at 0.5, and the SOFC current density reaches 8000 A/m^2. By maintaining these optimized parameter values, the system can operate more efficiently and sustainably.

6. Cycle evaluation of the system

To highlight the practical benefits and novelty of the proposed hybrid system, a comparison is made against standalone or conventional configurations, including a standalone SOFC system, a PVT-only system, and a biomass gasification system without solar preheating. This comparative analysis quantifies improvements in terms of gas composition, system efficiency, and output power.

In the case of biomass gasification, preheating with solar integration and syngas significantly enhances the quality of the produced gas. Table 9 shows the performance comparison between hybrid system and standalone alternatives. As shown in Table 9, without preheating (at 298 K), the mole fractions of the major components are $y_{H_2} = 0.1581$, $y_{CO} = 0.1480$, and $y_{CH_4} = 0.006$. However, when the gasifier is preheated using solar energy and syngas up to 900 K, these values improve to $y_{H_2} = 0.2279$, $y_{CO} = 0.2191$, and $y_{CH_4} = 0.012$. This enrichment in

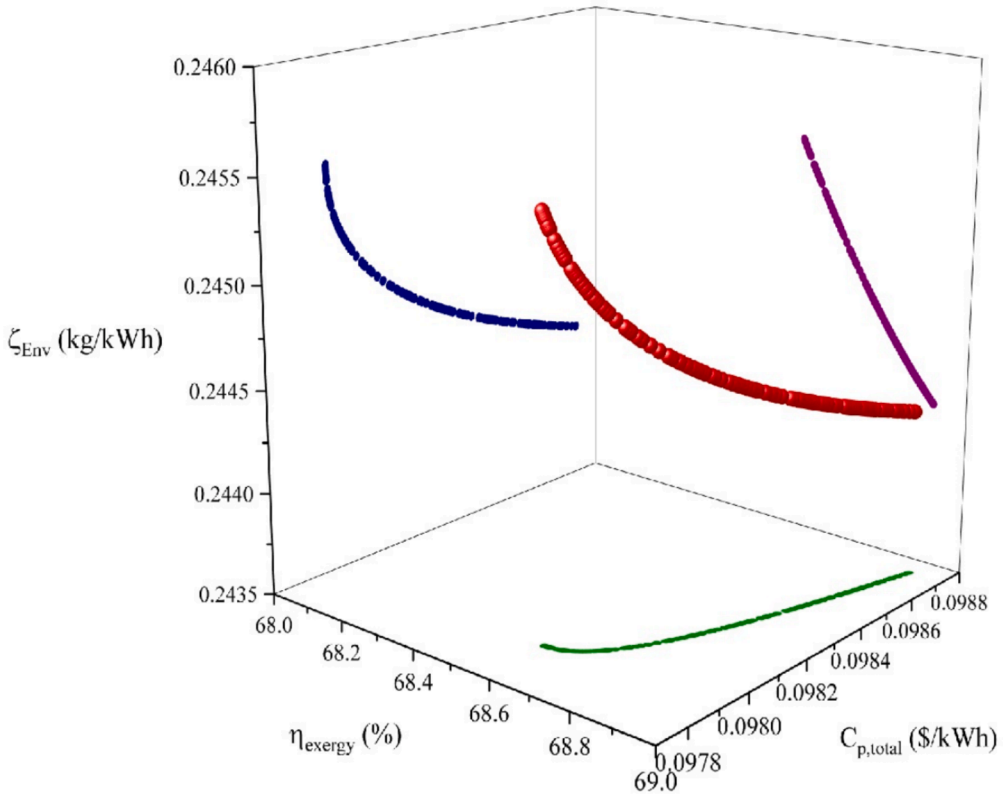

Fig. 16. The Pareto front diagram for third scenario.

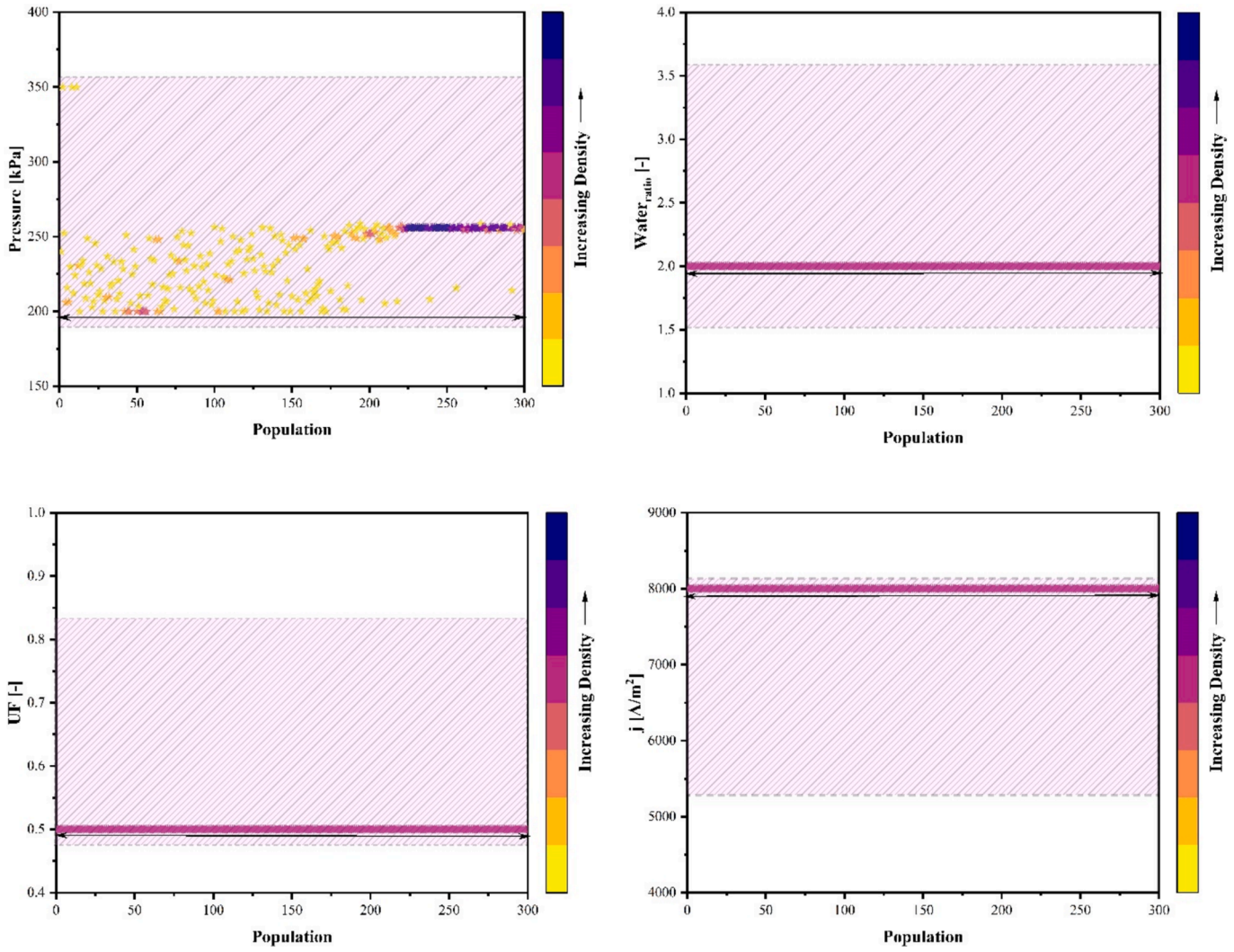

Fig. 17a–d. Scatter distribution for the decision variables for the first scenario.

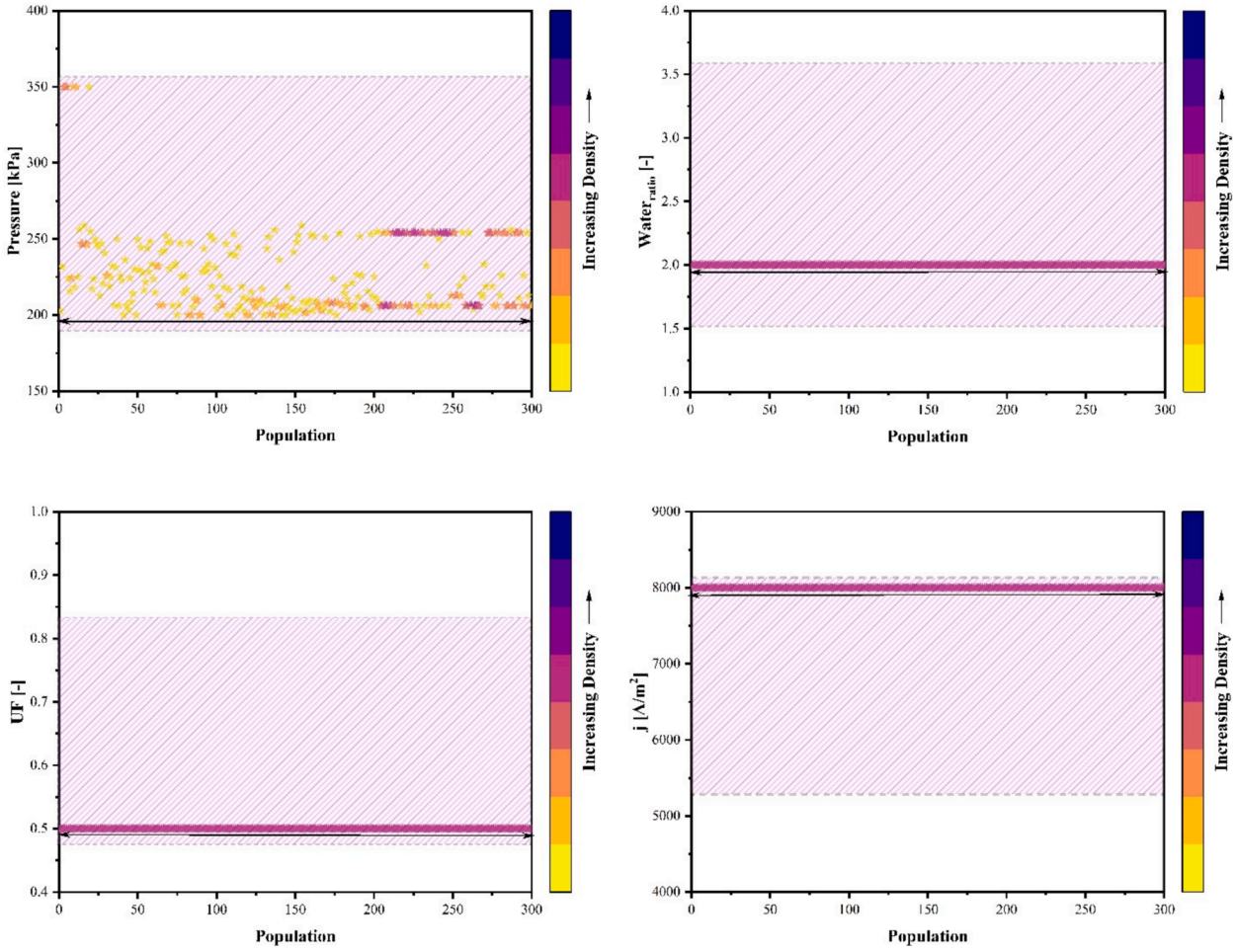

Fig. 17e–h. Scatter distribution for the decision variables for the second scenario.

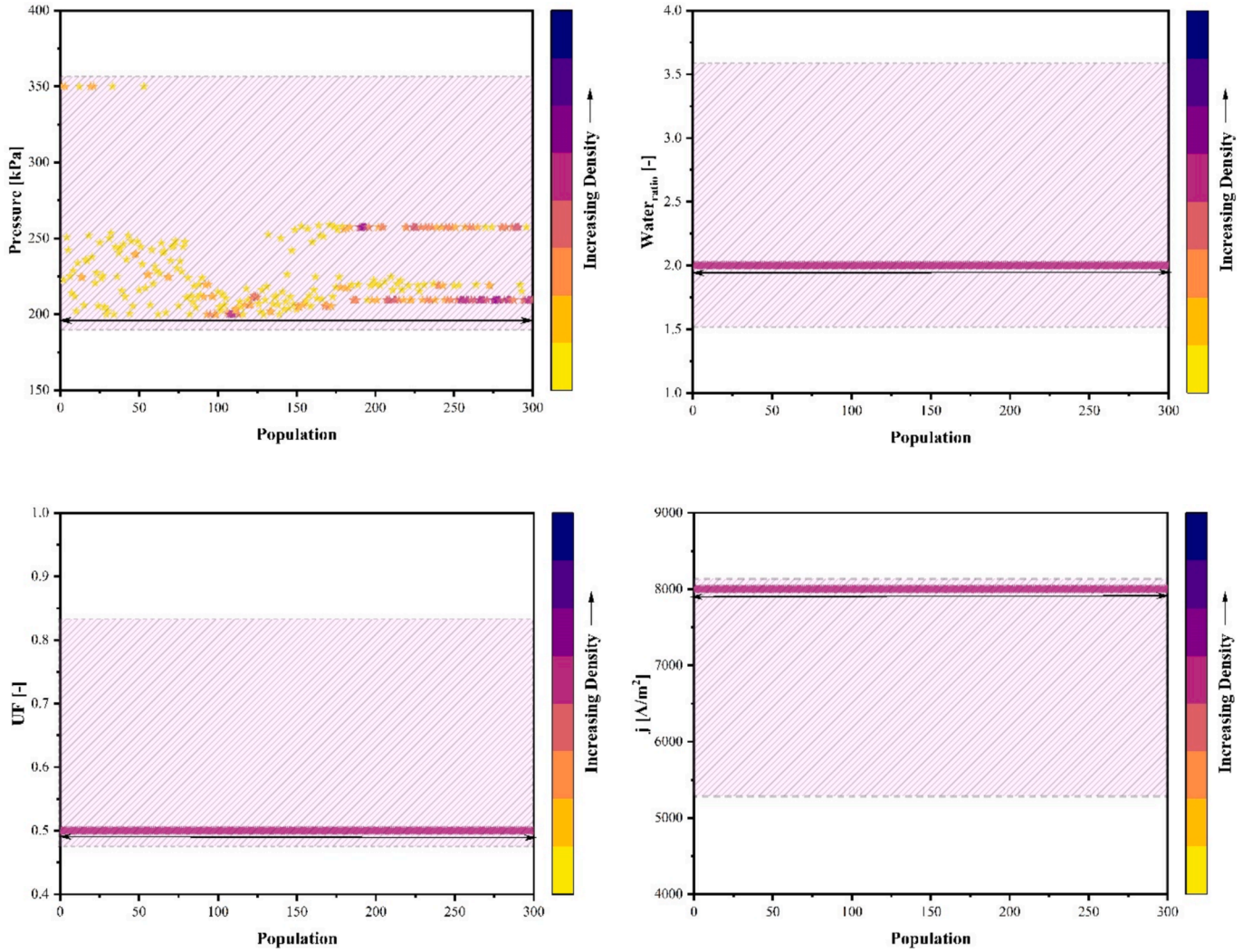

Fig. 17i–l. Scatter distribution for the decision variables for the third scenario.

Table 9
Performance comparison between hybrid system and standalone alternatives.

System Configuration	y_{H_2}	y_{CO}	y_{CH_4}	PVT Efficiency (%)	SOFC Output Power	Notable Benefits
Gasification at 298 K (no preheat)	0.1581	0.148	0.006	–	Lower	Baseline syngas quality
Gasification at 900 K (preheated)	0.2279	0.2191	0.0120	–	Higher	Enhanced syngas quality via solar heat
PVT without preheat unit	–	–	–	29.90	–	Only electricity production
PVT with preheat unit	–	–	–	30.38	–	Electricity and thermal utilization

hydrogen and carbon monoxide content leads to higher energy content in the syngas, directly benefiting the downstream SOFC performance. For the PVT subsystem, when operating without the contribution in preheating, the efficiency is 29.9 %. Upon integration with the solar preheating system, the efficiency increases to 30.38 %, showing improved utilization of solar energy. The SOFC unit also benefits from the improved syngas quality, resulting in enhanced output power. The increased hydrogen and CO availability from solar-assisted gasification contributes to higher electrochemical reaction rates within the fuel cell, thereby improving its performance and supporting the system's overall efficiency.

This comparison confirms that the integration of solar preheating and hybridization in the proposed system results in superior performance, increased efficiency, and supports the novelty of the configuration.

7. Conclusion

This research investigates an innovative hybrid system that incorporates a photovoltaic thermal (PVT) unit for air preheating, and steam injection into the gasifier to improve gasification efficiency and optimization of a solid oxide fuel cell (SOFC). Additionally, the PVT unit provides heat for the gasification agent and electricity to a proton exchange membrane (PEM) electrolyzer for producing hydrogen and oxygen. The system's performance was assessed through detailed energy, exergy, exergoeconomic, and environmental analyses. The primary findings of this study are as follows:

- The overall energy efficiency is determined to be 55.03 %, while the exergy efficiency is 50.64 %, demonstrating the system's effective utilization of energy and exergy resources. The products' estimated cost is 0.125 $/kWh, highlighting the system's economic feasibility.

- The system demonstrates effective exergy balance, with solar and biomass exergy significantly enhancing SOFC power generation. Waste heat utilization reduces exergy destruction in the SOFC, while the highest exergy losses occur in the PVT system.
- Based on the parametric study, increasing the water-to-biomass ratio improves hydrogen and carbon monoxide production but reduces energy efficiency, while higher Fuel Utilization Factor (UF) and current densities enhance power output but decrease energy efficiency and increase environmental and cost impacts.
- Optimal results include a total specific cost of 0.098 $/kWh, an energy efficiency of 74.88 %, and an environmental impact factor of 0.244 kg/kWh, providing a balanced framework for system optimization.

This study demonstrates the potential of the proposed hybrid system in achieving enhanced energy efficiency, cost-effectiveness, and reduced environmental impact, providing valuable insights for future renewable energy applications.

CRediT authorship contribution statement

Shayan Sharafi Laleh: Writing – original draft, Visualization, Validation, Software, Resources, Project administration, Methodology, Investigation, Formal analysis, Data curation, Conceptualization. **Haniyeh Sadat Rezaei Mousavi:** Writing – original draft, Visualization, Validation, Supervision, Software, Resources, Methodology, Investigation, Formal analysis, Data curation, Conceptualization. **Shayan Rabet:** Writing – original draft, Visualization, Validation, Supervision, Software, Resources, Project administration, Methodology, Investigation, Formal analysis, Data curation, Conceptualization. **Farnaz Nojavan:** Writing – original draft, Visualization, Validation, Software, Resources, Project administration, Methodology, Investigation, Formal analysis, Data curation, Conceptualization. **Mortaza Yari:** Writing – original draft, Visualization, Validation, Supervision, Software, Resources, Project administration, Methodology, Investigation, Formal analysis, Data curation, Conceptualization. **Saeed Soltani:** Writing – original draft, Visualization, Validation, Supervision, Software, Resources, Project administration, Methodology, Investigation, Formal analysis, Data curation, Conceptualization.

Declaration of competing interest

The authors declare that they have no known competing financial interests or personal relationships that could have appeared to influence the work reported in this paper.

Appendix

A. Balance for components.

Table A1
Equations of energy balance of components [40,41].

Component	Energy balance equation
AC	$\dot{W}_{AC} = \dot{m}_{19}h_{19} - \dot{m}_{18}h_{18}$
Afterburner	$\dot{m}_{22}h_{22} + \dot{m}_{17}h_{17} = \dot{m}_{23}h_{23}$
Cleaner	$\dot{m}_{7}h_{7} = \dot{m}_{8}h_{8} + \dot{m}_{imp}h_{imp}$
Condenser	$\dot{m}_{26}h_{26} = \dot{m}_{27}h_{27}$
Gasifier	$\dot{m}_{30}h_{30} + \dot{m}_{3}h_{3} + \dot{m}_{12}h_{12} = \dot{m}_{4}h_{4}$
GT1	$\dot{W}_{GT1} = \dot{m}_{23}h_{23} - \dot{m}_{24}h_{24}$
GT2	$\dot{W}_{GT2} = \dot{m}_{25}h_{25} - \dot{m}_{26}h_{26}$
HX1	$\dot{m}_{2}h_{2} + \dot{m}_{5}h_{5} = \dot{m}_{3}h_{3} + \dot{m}_{6}h_{6}$
HX2	$\dot{m}_{11}h_{11} + \dot{m}_{4}h_{4} = \dot{m}_{12}h_{12} + \dot{m}_{5}h_{5}$
HX3	$\dot{m}_{6}h_{6} + \dot{m}_{31}h_{31} = \dot{m}_{7}h_{7} + \dot{m}_{32}h_{32}$
HX4	$\dot{m}_{8}h_{8} + \dot{m}_{9}h_{9} = \dot{m}_{10}h_{10} + \dot{m}_{13}h_{13}$
HX5	$\dot{m}_{14}h_{14} + \dot{m}_{16}h_{16} = \dot{m}_{15}h_{15} + \dot{m}_{17}h_{17}$
HX6	$\dot{m}_{19}h_{19} + \dot{m}_{21}h_{21} = \dot{m}_{20}h_{20} + \dot{m}_{22}h_{22}$
HX7	$\dot{m}_{24}h_{24} + \dot{m}_{28}h_{28} = \dot{m}_{25}h_{25} + \dot{m}_{29}h_{29}$
Pump	$\dot{W}_{Pump} = \dot{m}_{28}h_{28} - \dot{m}_{27}h_{27}$
Syngas Comp	$\dot{W}_{syngasC} = \dot{m}_{14}h_{14} - \dot{m}_{13}h_{13}$

.

Table A2
Equations of exergy balance of components [40,41].

Component	Exergy balance equation
AC	$\dot{E}_{18} + \dot{W}_{AC} = + \dot{E}_{19} + \dot{E}_{D,AC}$
Afterburner	$\dot{E}_{22} + \dot{E}_{17} = \dot{E}_{23} + \dot{E}_{D,AB}$
Cleaner	$\dot{E}_{7} = \dot{E}_{8} + \dot{E}_{impurities} + \dot{E}_{D,cleaner}$
Condenser	$\dot{E}_{26} = \dot{E}_{27} + \dot{E}_{D,Condenser}$
Gasifier	$\dot{E}_{30} + \dot{E}_{3} + \dot{E}_{12} = \dot{E}_{4} + \dot{E}_{D,total}$
GT1	$\dot{E}_{23} = \dot{E}_{24} + \dot{W}_{GT1} + \dot{E}_{D,GT1}$
GT2	$\dot{E}_{25} = \dot{E}_{26} + \dot{W}_{GT2} + \dot{E}_{D,GT2}$
HX1	$\dot{E}_{2} + \dot{E}_{5} = \dot{E}_{3} + \dot{E}_{6} + \dot{E}_{D,HX1}$
HX2	$\dot{E}_{4} + \dot{E}_{11} = \dot{E}_{5} + \dot{E}_{12} + \dot{E}_{D,HX2}$
HX3	$\dot{E}_{6} + \dot{E}_{31} = \dot{E}_{7} + \dot{E}_{32} + \dot{E}_{D,HX3}$
HX4	$\dot{E}_{8} + \dot{E}_{9} = \dot{E}_{13} + \dot{E}_{10} + \dot{E}_{D,HX4}$

(*continued on next page*)

Table A2 (*continued*)

Component	Exergy balance equation
HX5	$\dot{E}_{14} + \dot{E}_{16} = \dot{E}_{15} + \dot{E}_{17} + \dot{E}_{D,HX5}$
HX6	$\dot{E}_{19} + \dot{E}_{21} = \dot{E}_{20} + \dot{E}_{22} + \dot{E}_{D,HX6}$
HX7	$\dot{E}_{24} + \dot{E}_{18} = \dot{E}_{29} + \dot{E}_{25} + \dot{E}_{D,Boiler}$
PEM	$\dot{E}_{32} + \dot{W}_{PVT} = \dot{E}_{32'} + \dot{E}_{33} + \dot{E}_{34} + \dot{E}_{D,HX3}$
Pump	$\dot{E}_{27} + \dot{W}_{Pump} = \dot{E}_{28} + \ + \dot{E}_{D,GT1}$
PVT	$\dot{E}_{1} + \dot{E}_{solar} = \dot{E}_{2} + \dot{W}_{PVT} + \dot{E}_{D,PVT}$
SOFC	$\dot{E}_{15} + \dot{E}_{20} = \dot{E}_{16} + \dot{E}_{21} + \dot{W}_{SOFC} + \dot{E}_{D,total}$
Syngas Comp	$\dot{E}_{13} + \dot{W}_{syngasC} = \dot{E}_{14} + \dot{E}_{D,syngasC}$

B. Cost functions.

Table B1
Cost Functions of components.

Component	Cost function	Reference
SOFC sub-system Fuel compressor	$Z_{fuelcomp} = 91562\left(\frac{\dot{W}_{fuelcomp}}{455}\right)^{0.67}$	[32]
Fuel-rich combustion chamber	$Z_{CC} = \frac{46.08\dot{m}_{17a}}{0.955 - \left(\frac{P_{20}}{P_{17}}\right)}\left(1 + e^{0.018T_{20} - 26.4}\right)$	[32]
Heat exchanger	$Z_{HEX} = 130\left(\frac{A_{preheater}}{0.093}\right)^{0.78}$	[32]
SOFC	$Z_{SOFC} = A_a N_{FC}(2.96T_{stack} - 1907)$	[32]
Inverter	$Z_{inv} = 100000\left(\frac{\dot{W}_{SOFC,DC}}{500}\right)^{0.7}$	[32]
Afterr-burner	$Z_{AB} = \frac{46.08\dot{m}_{23}}{0.955 - \left(\frac{P_{24}}{P_{23}}\right)}\left(1 + e^{0.018T_{24} - 26.4}\right)$	[32]
Gas turbine	$Z_{GT} = \frac{479.34\dot{m}_{24}}{0.92 - \eta_{GT}} ln\left(\frac{P_{24}}{P_{25}}\right)(1 + exp(0.036T_{24} - 54.4))$	[46]
PEM	$Z_{PEM} = 1000\ \dot{W}_{PEM}$ *	[33]
PVT	$ZPVT = 310\ n_x n_y bL$** $(n_x = 6, n_y = 6)$	[33]
ST	$Z_{ST} = 4405(Z_{ST})^{0.7}$	[33]
SP	$Z_{SP} = 1120(Z_{SP})^{0.8}$	[33]
HRSG	$Z_{ST} = 2143(a_{HRSG})^{0.514}$	[33]

* Covered are the fees for the HX and O_2 separator.
** n_x and n_y denote the cell count in the PVT's span (b) and height (L).

Data availability

The authors are unable or have chosen not to specify which data has been used.

References

[1] Pan J, Yang Y, Lei J, Huang X. Thermodynamic analysis of an integrated reversible solid oxide fuel cell system. Energy Convers Manag X 2023;20:100484. https://doi.org/10.1016/j.ecmx.2023.100484.

[2] Zhou Z, Dhahad HA, Almohana AI, Almojil SF, Alali AF, Anqi AE, et al. Multi-objective optimization of a clean combined system based gasifier-solid oxide fuel cell. Int J Hydrogen Energy 2022;47:18648–62. https://doi.org/10.1016/j.ijhydene.2022.04.034.

[3] Feng Y, Qu J, Zhu Y, Wu B, Wu Y, Xiao Z, et al. Progress and prospect of the novel integrated SOFC-ICE hybrid power system: system design, mass and heat integration, system optimization and techno-economic analysis. Energy Convers Manag X 2023;18:100350. https://doi.org/10.1016/j.ecmx.2023.100350.

[4] Taylor JD, Herdman CM, Wu BC, Wally K, Rice SF. Hydrogen production in a compact supercritical water reformer. Int J Hydrogen Energy 2003;28:1171–8. https://doi.org/10.1016/S0360-3199(02)00291-4.

[5] Nourbakhsh H, Khani Y, Zamaniyan A, Bahadoran F. Hydrogen and syngas production through dynamic chemical looping reforming-decomposition of methane. Int J Hydrogen Energy 2022;47:9835–52. https://doi.org/10.1016/j.ijhydene.2022.01.066.

[6] Rakousky C, Reimer U, Wippermann K, Kuhri S, Carmo M, Lueke W, et al. Polymer electrolyte membrane water electrolysis: restraining degradation in the presence of fluctuating power. J Power Sources 2017;342:38–47. https://doi.org/10.1016/j.jpowsour.2016.11.118.

[7] Nabat MH, Zeynalian M, Razmi AR, Arabkoohsar A, Soltani M. Energy, exergy, and economic analyses of an innovative energy storage system; liquid air energy storage (LAES) combined with high-temperature thermal energy storage (HTES). Energy Convers Manag 2020;226:113486. https://doi.org/10.1016/j.enconman.2020.113486.

[8] Fragiacomo P, Genovese M. Technical-economic analysis of a hydrogen production facility for power-to-gas and hydrogen mobility under different renewable sources in Southern Italy. Energy Convers Manag 2020;223:113332. https://doi.org/10.1016/j.enconman.2020.113332.

[9] Li N, Araya SS, Kær SK. Investigating low and high load cycling tests as accelerated stress tests for proton exchange membrane water electrolysis. Electrochim Acta 2021;370:137748. https://doi.org/10.1016/j.electacta.2021.137748.

[10] Shakeri A, Eshghi H, Salek F, Babaie M. Energy assessment for integration of concrete thermal energy storage with low-grade solar power generation system. Renew Energy 2023;218:119249. https://doi.org/10.1016/j.renene.2023.119249.

[11] Kumar A, Tiwari AK, Said Z. A comprehensive review analysis on advances of evacuated tube solar collector using nanofluids and PCM. Sustain Energy Technol Assessments 2021;47:101417. https://doi.org/10.1016/j.seta.2021.101417.

[12] Atiz A, Karakilcik H, Erden M, Karakilcik M. Assessment of electricity and hydrogen production performance of evacuated tube solar collectors. Int J Hydrogen Energy 2019;44:14137–44. https://doi.org/10.1016/j.ijhydene.2018.09.100.

[13] Demir ME, Dincer I. Development of a hybrid solar thermal system with TEG and PEM electrolyzer for hydrogen and power production. Int J Hydrogen Energy 2017;42:30044–56. https://doi.org/10.1016/j.ijhydene.2017.09.001.

[14] Ma Y, Zhao M, Bai F, Yu R, Liu L, Wang J. Numerical simulation and experimental verification of solar PVT coupled PEM electrolyzer system for hydrogen production. Fuel 2024;365:131323. https://doi.org/10.1016/j.fuel.2024.131323.
[15] Soyturk G, Kizilkan O, Ezan MA, Colpan CO. Design, modeling, and analysis of a PV/T and PEM fuel cell based hybrid energy system for an off-grid house. Int J Hydrogen Energy 2024;67:1181–93. https://doi.org/10.1016/j.ijhydene.2023.11.291.
[16] Liu L, Duan L, Zheng N, Wang Q, Zhang M, Xue D. Thermodynamic performance evaluation of a novel solar-assisted multi-generation system driven by ammonia-fueled SOFC with anode outlet gas recirculation. Energy 2024;294:130845. https://doi.org/10.1016/j.energy.2024.130845.
[17] Fang Y, Li X, Ascher S, Li Y, Dai L, Ruan R, et al. Life cycle assessment and cost benefit analysis of concentrated solar thermal gasification of biomass for continuous electricity generation. Energy 2023;284:128709. https://doi.org/10.1016/j.energy.2023.128709.
[18] Forootan MM, Ahmadi A. Machine learning-based optimization and 4E analysis of renewable-based polygeneration system by integration of GT-SRC-ORC-SOFC-PEME-MED-RO using multi-objective grey wolf optimization algorithm and neural networks. Renew Sustain Energy Rev 2024;200:114616. https://doi.org/10.1016/j.rser.2024.114616.
[19] Zhao H, Du H, Peng Z, Zhang T. Thermodynamic performance analysis of a novel energy storage system consist of asymmetric PEMEC and SOFC combined cycle. Energy Convers Manag 2023;286:117077. https://doi.org/10.1016/j.enconman.2023.117077.
[20] Yang S, Wang G, Liu Z, Deng C, Xie N. Energy, exergy and exergo-economic analysis of a novel SOFC based CHP system integrated with organic Rankine cycle and biomass co-gasification. Int J Hydrogen Energy 2024;53:1155–69. https://doi.org/10.1016/j.ijhydene.2023.12.150.
[21] Ogorure OJ, Heberle F, Brüggemann D. Thermo-economic analysis and multi-criteria optimization of an integrated biomass-to-energy power plant. Renew Energy 2024;224:120112. https://doi.org/10.1016/j.renene.2024.120112.
[22] Abedinia O, Shakibi H, Shokri A, Sobhani B, Sobhani B, Yari M, et al. Optimization of a syngas-fueled SOFC-based multigeneration system: enhanced performance with biomass and gasification agent selection. Renew Sustain Energy Rev 2024;199:114460. https://doi.org/10.1016/j.rser.2024.114460.
[23] Yin J, Ning X, Ma Y. Study on the synergistic effect of sludge-based supercritical water gasification-supercritical water oxidation-solid oxide fuel cell system for power generation and solar thermal utilization. Int J Hydrogen Energy 2025;109:306–24. https://doi.org/10.1016/j.ijhydene.2025.01.411.
[24] Zheng N, Zhang H, Duan L, Wang Q. Comprehensive sustainability assessment of a novel solar-driven PEMEC-SOFC-based combined cooling, heating, power, and storage (CCHPS) system based on life cycle method. Energy 2023;265:126343. https://doi.org/10.1016/j.energy.2022.126343.
[25] Saberi Mehr A, Ilkhani M, Sabernia S, Nooshmand S, Ebrahimpour A, Heydari B. Thermodynamic modelling and optimisation of a green hydrogen-blended syngas-fueled integrated PV-SOFC system. Appl Therm Eng 2024;236:121506. https://doi.org/10.1016/j.applthermaleng.2023.121506.
[26] Salari A, Shakibi H, Soleimanzade MA, Sadrzadeh M, Hakkaki-Fard A. Application of machine learning in evaluating and optimizing the hydrogen production performance of a solar-based electrolyzer system. Renew Energy 2024;220:119626. https://doi.org/10.1016/j.renene.2023.119626.
[27] Tera I, Zhang S, Liu G. A conceptual hydrogen, heat and power polygeneration system based on biomass gasification, SOFC and waste heat recovery units: energy, exergy, economic and emergy (4E) assessment. Energy 2024;295:131015. https://doi.org/10.1016/j.energy.2024.131015.
[28] Ishaq H, Dincer I. Design and performance evaluation of a new biomass and solar based combined system with thermochemical hydrogen production. Energy Convers Manag 2019;196:395–409. https://doi.org/10.1016/j.enconman.2019.05.100.
[29] Moharramian A, Soltani S, Rosen MA, Mahmoudi SMS, Bhattacharya T. Modified exergy and modified exergoeconomic analyses of a solar based biomass co-fired cycle with hydrogen production. Energy 2019;167:715–29. https://doi.org/10.1016/j.energy.2018.10.197.
[30] Ahmadi P, Dincer I, Rosen MA. Energy and exergy analyses of hydrogen production via solar-boosted ocean thermal energy conversion and PEM electrolysis. Int J Hydrogen Energy 2012;38:1795–805. https://doi.org/10.1016/j.ijhydene.2012.11.025.
[31] Yang C, Guo R, Jing X, Li P, Yuan J, Wu Y. Degradation mechanism and modeling study on reversible solid oxide cell in dual-mode — a review. Int J Hydrogen Energy 2022;47:37895–928. https://doi.org/10.1016/j.ijhydene.2022.08.240.
[32] Sadeghi M, Chitsaz A, Mahmoudi SMS, Rosen MA. Thermoeconomic optimization using an evolutionary algorithm of a trigeneration system driven by a solid oxide fuel cell. Energy 2015;89:191–204. https://doi.org/10.1016/j.energy.2015.07.067.
[33] Massardo A, Lubelli F. Internal reforming solid oxide fuel cell-gas turbine combined cycles (IRSOFC-GT): part a—cell model and cycle thermodynamic analysis. J Eng Gas Turbines Power-Trans ASME 2000;122:27–35. https://doi.org/10.1115/1.483187.
[34] Bossel UG, Dubal L. Facts and figures, an International Energy Agency SOFC task report 1992.
[35] Kim J, Virkar AV, Fung K, Mehta K, Singhal SC. Polarization effects in intermediate temperature, anode-supported solid oxide fuel cells. J Electrochem Soc 1999;146:69. https://doi.org/10.1149/1.1391566.
[36] Chan SH, Low CF, Ding OL. Energy and exergy analysis of simple solid-oxide fuel-cell power systems. J Power Sources 2002;103. https://doi.org/10.1016/S0378-7753(01)00842-4.
[37] Zainal ZA, Ali R, Lean CH, Seetharamu KN. Prediction of performance of a downdraft gasifier using equilibrium modeling for different biomass materials. Energy Convers Manag 2001;42:1499–515.
[38] Soltani S, Mahmoudi SMS, Yari M, Rosen MA. Thermodynamic analyses of an externally fired gas turbine combined cycle integrated with a biomass gasification plant. Energy Convers Manag 2013;70:107–15. https://doi.org/10.1016/j.enconman.2013.03.002.
[39] Falcão D, Pinto A. A review on PEM electrolyzer modelling: guidelines for beginners. J Clean Prod 2020;261:121184. https://doi.org/10.1016/j.jclepro.2020.121184.
[40] Bejan A, Tsatsaronis G, Moran MJ. Thermal design and optimization. John Wiley & Sons; 1995.
[41] Bejan A. Advanced engineering thermodynamics. John Wiley & Sons; 2016.
[42] Gholamian E, Mehr AS, Yari M, Carton JG. Dynamic simulation and techno-economic assessment of hydrogen utilization in dual fuel (Hydrogen/biogas) micro gas turbine systems for a wastewater treatment plant. Process Saf Environ Prot 2023;169:220–37. https://doi.org/10.1016/j.psep.2022.10.045.
[43] Tao G, Armstrong T, Virkar A. Intermediate temperature solid oxide fuel cell (IT-SOFC) research and development activities at MSRI. Ninet. Annu. ACERC&ICES Conf., Provo, UT; 2005.
[44] Yari M, Mehr AS, Mahmoudi SMS, Santarelli M. A comparative study of two SOFC based cogeneration systems fed by municipal solid waste by means of either the gasifier or digester. Energy 2016;114:586–602. https://doi.org/10.1016/j.energy.2016.08.035.
[45] Ioroi T, Yasuda K, Siroma Z, Fujiwara N, Miyazaki Y. Thin film electrocatalyst layer for unitized regenerative polymer electrolyte fuel cells. J Power Sources 2002;112:583–7. https://doi.org/10.1016/S0378-7753(02)00466-4.
[46] Wang S, Liu C, Li J, Sun Z, Chen X, Wang X. Exergoeconomic analysis of a novel trigeneration system containing supercritical CO2 Brayton cycle, organic Rankine cycle and absorption refrigeration cycle for gas turbine waste heat recovery. Energy Convers Manag 2020;221:113064.